Astronomy & Astrophysics manuscript no. output
November 19, 2019

The Spectrometer/Telescope for Imaging X-rays (STIX)

Säm Krucker[1,2] G. J. Hurford[1,2] O. Grimm[1,4] D. Casadei[1] L. Etesi[1] A. Csillaghy[1] A. O. Benz[1] S. Kögl[1] G. Arnold[1] F. Molendini[1] P. Orleanski[1] H.-P Gröbelbauer[1] D. Schori[1] H. Xiao[1] M. Kuhar[1] S. Kobler[1] L. Iseli[1] H. J. Wiehl[1] N. Hochmuth[1] S. Marcin[1] S. Felix[1] L. Kleint[1] M. Battaglia[1] M. Bednarzik[3] R. Resanovič,[3] K. R. Skup,[5] A. Cichocki[5] W. Bujwan[5] R. Graczyk[5] M. Stolarski[5] M. Michalska[5] W. Nowosielski[5] M. Mosdorf[5] K. Seweryn[5] A. Białek[5] P. Osica[5] J. Sylwester[6] M. Kowalinski[6] D. Ścisłowski[6] T. Mrozek[6] P. Podgorski[6] A. Meuris[7] O. Limousin[7] S. Brun[7] N. Vilmer[8] S. Musset[8,9] F. Farnik[10] J. Kasparova[10] G. Mann[11] H. Önel[11] A. Warmuth[11] F. Dionies[11] S. Bauer[11] J. Rendtel[11] M. Woche[11] A. Veronig,[12] O. Dickson,[12] P. T. Gallagher,[13] S. Maloney[13] M. Byrne[13] M. Piana[14] A. M. Massone[14] R. A. Schwartz[15,16,12,17] B. R. Dennis[15] H. F. van Beek, R. P. Lin[2]

[1] University of Applied Sciences Northwestern Switzerland
[2] Space Sciences Laboratory, University of California, Berkeley, USA
[3] Paul Scherrer Institute, Villingen, Switzerland
[4] ETH Zürich, Switzerland
[5] Space Research Center, Warsaw, Poland
[6] Space Research Center, Wroclaw, Poland
[7] CEA-IRFU, France
[8] LESIA, Observatoire de Paris, France
[9] University of Minnesota, USA
[10] Astronomical Institute, The Czech Academy of Sciences, Ondřejov, Czech Republic
[11] Leibniz-Institut für Astrophysik Potsdam, Germany
[12] University of Graz, Austria
[13] Trinity Collegue Dublin, Ireland
[14] Universita di Genova, Italy
[15] Goddard Space Flight Center, USA
[16] American University, Washington, USA
[17] Dublin Institute for Advanced Studies, Dublin, Ireland

Received November 30, 2019; accepted

ABSTRACT

Aims. The Spectrometer Telescope for Imaging X-rays (STIX) onboard Solar Orbiter is a hard X-ray imaging spectrometer covering the energy range from 4 to 150 keV. STIX observes hard X-ray bremsstrahlung emissions from solar flares providing diagnostics of the hottest ($\gtrsim$10 MK) flare plasma and simultaneously quantifies the spectrum and energy content of flare-accelerated non-thermal electrons.
Methods. To accomplish this, STIX applies an indirect bigrid Fourier-imaging technique using a set of tungsten grids (at pitches from 0.038 to 1 mm) in front of 32 coarsely pixelated CdTe detectors to provide information on angular scales from 7 to 180 arcsec with 1 keV energy resolution (at 6 keV). The indirect imaging concept of STIX with its intrinsically low telemetry requirement is very well suited for the limited resources available to the Solar Orbiter payload. To further reduce the downlinked data volume, STIX data is binned the onboard into 32 selectable energy bins and time bins of typical duration of 1 second).
Results. Through hard X-ray diagnostics, STIX plays an important role in enabling Solar Orbiter to understand how solar eruptions produce energetic particles that fill the inner heliosphere. In this way, STIX links the remote and in-situ instruments of the Solar Orbiter mission.

Key words. Instrumentation: miscellaneous Sun: X-rays – Sun: flares

1. Introduction

The Spectrometer/Telescope for Imaging X-ray (STIX) complements the Solar Orbiter mission with hard X-ray imaging spectroscopy measurements providing diagnostics of the hottest ($\gtrsim$10 MK) thermal plasmas in the solar corona and information of non-thermal electrons that are accelerated during solar flares. The instrument applies Fourier-transform imaging technique similar to that used successfully by the Hard X-ray Telescope (HXT) on the Japanese Yohkoh mission, and related to that used for the Reuven Ramaty High Energy Solar Spectroscopic Imager (RHESSI) mission. Hard X-ray spectroscopy in the 4 to 150 keV at 1 keV resolution is achieved by the use of passively cooled Cadmium Telluride (CdTe) X-ray detectors. The indirect imaging concept of STIX is very well suited to the limited mass, power and telemetry resources available for the Solar Orbiter payload. For example, each STIX image can be transmitted with as little as 100 bytes.

The next chapter briefly highlights the core of the STIX science objectives with the general Solar Orbiter science. Afterwards, the instrument overview is presented in Section 3 followed by chapters on the instrument imaging (Section 4), detec-

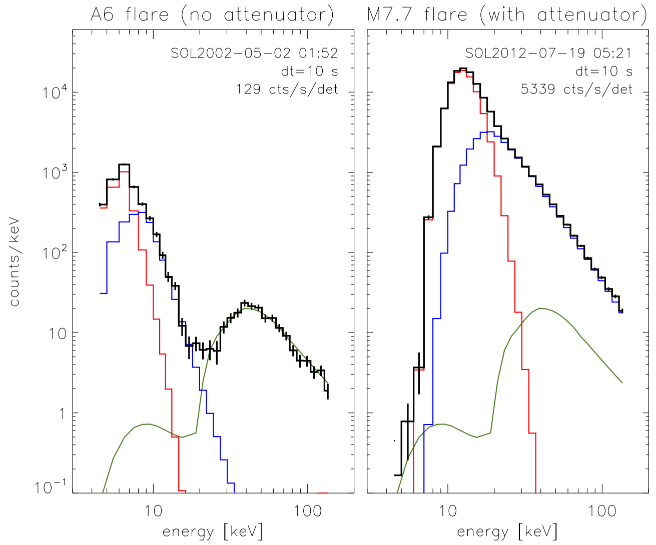

Fig. 1: Typical STIX HXR count spectra, for two real flares (GOES A6 and M7.7), shown as 10-second accumulations in STIX science energy channels. The black plot is the detector-summed count spectra which includes the thermal component, nonthermal component and predicted background (red, blue and green plots respectively).

tor and electronics (Section 5), and onboard data handling (Section 6). The STIX operation concept, data products and analysis considerations are summarized in Section 7.

2. Science objectives

The dominate emission mechanism in the STIX hard X-ray energy range is bremsstrahlung produced when energetic electrons decelerate in the solar corona as they encounter ambient protons. Only the highest energy electrons of the distribution have generally enough energy to produce bremsstrahlung above the STIX lower energy range. The low energy limit of STIX at 4 keV corresponds to a mean electron energy of a thermal population of ~ 45 MK; a value that is only very rarely achieved in solar flares. STIX with it is energy range from 4 to 150 keV therefore provide information of the tail of the electron distribution giving diagnostics of the most energetic electrons. Hence, hard X-ray emissions are an ideal diagnostics of the hottest plasmas in solar flares and for non-thermal tails seen at energies above the hottest thermal population.

Typical hard X-ray flare spectra is shown in Figure 1 with a thermal distribution seen best at the lower energy end, while the high energy end typically above 30 keV is produced by non-thermal electrons. For smaller flare which tend to be cool, the energy at above which non-thermal emission is seen is generally lower, and can reach values below 10 keV. As bremsstrahlung emission mechanism is rather well understood, the observed spectra provides quantitative diagnostics.

In summary, solar flare hard X-ray observations give quantitative measurements of energy release processes in solar flares. The remote-sensing X-ray measurements made with STIX will determine the intensity, spectrum, timing, and location of accelerated electrons near the Sun. Simultaneously, the size, density, temperature, and energy content of the flare-heated plasma are determined. By using this set of diagnostics, STIX plays an important role in enabling Solar Orbiter to achieve two of its major science goals of (1) understanding the acceleration of electrons at the Sun and their transport into interplanetary space and (2) determining the magnetic connection of the Solar Orbiter back to the Sun. In this way, STIX provides an important link between the remote and in-situ instruments of the Solar Orbiter mission.

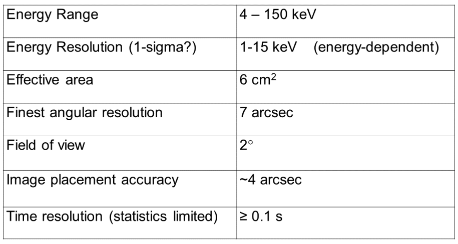

Energy Range	4 – 150 keV
Energy Resolution (1-sigma?)	1-15 keV (energy-dependent)
Effective area	6 cm^2
Finest angular resolution	7 arcsec
Field of view	2°
Image placement accuracy	~4 arcsec
Time resolution (statistics limited)	≥ 0.1 s

Fig. 2: Table 1. STIX Performance Summary

3. Instrument overview

The STIX instrument provides imaging spectroscopy of solar flare x-ray emission. Instrument performance is summarized in Table 1.

The hardware consists of three main subsystems (Figure 3):

- A pair of X-ray transparent entrance windows, independently mounted in the heat shield of Solar Orbiter;
- An imager with two widely separated grids, independently mounted on the s/c Y panel, and containing key elements of an aspect system;
- A Detector/Electronics Module (DEM), mounted behind the imager, containing electronics and cadmium telluride (CdTe) detectors.

The 5 to 150 keV energy range covers thermal and non-thermal X-ray emission with sufficient energy resolution to enable physical parametrization of the of the steep X-ray spectra. However, it does not include the higher energies needed to study gamma-ray emission from accelerated ions. The field of view for both imaging and spectroscopy covers the full Sun, even at perihelion, with sufficient angular resolution to separate and characterize individual footpoints. Note that the spatial resolution and sensitivity increase significantly as the s/c approaches the Sun.

As an imaging spectrometer (as opposed to an imager and a spectrometer), the spectral diagnostics and time behavior can be applied to individual spatial features.

The following paragraphs introduce the individual subsystems which are then described in more detail in subsequent sections.

3.1. Window

The STIX X-ray windows (Figure /,/refFig:STIX) play two roles. First, they are prime elements in the instrument thermal control system, reflecting and reradiating most of the incident radiation, so as to limit the optical and IR solar flux seen by the instrument itself and the s/c interior.

Second, it serves to preferentially absorb the intense flux of low energy X-rays that would otherwise result in excessive count rates, pulse pileup and dead time in the detectors during intense flares. Using low-Z materials (primarily optical grade beryllium). the thermally-effective window has X-ray absorption properties to permit observations down to 4 keV. In terms of mounting, the 2-mm thick front window are attached via 6

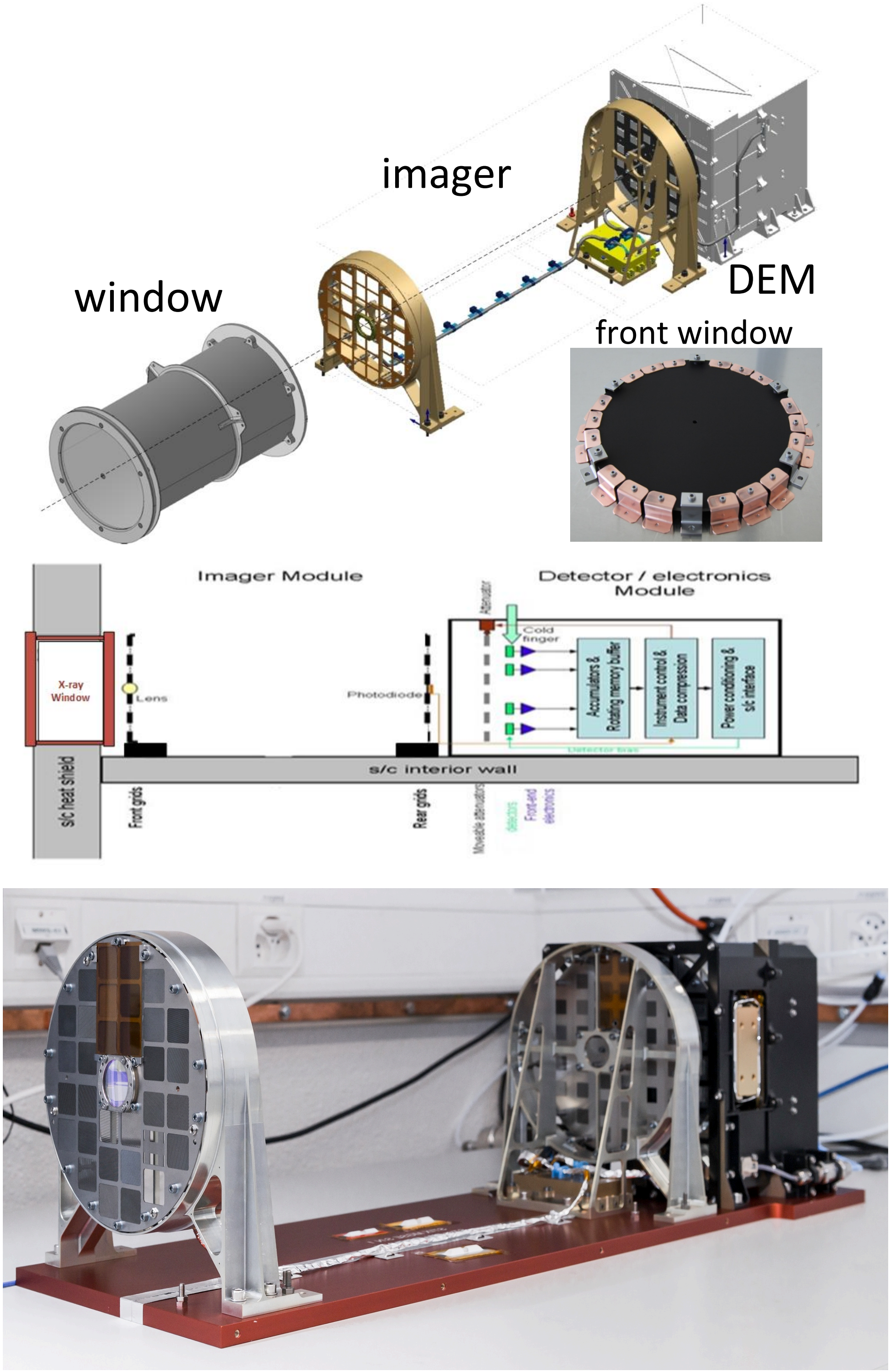

Fig. 3: Drawing, functional and photographic views of the STIX instrument, as described in the text. The inset (top) shows the front window, the 6 decoupling springs and copper thermal straps.

decoupled springs to a feedthrough provided by Solar Orbiter. The 1-mm thick rear window is directly attached to the rear of the heatshield feedthrough (Figure 3). To increase the margin on the thermal design, the front window is coated with Solar Black, the same coating that used on for the Solar Orbiter heatshield. The front and rear windows have 5 and 25 mm diameter open apertures respectively for use by the STIX aspect system.

3.2. Imager

High-resolution solar hard X-ray imaging within the mass and volume constraints of Solar Orbiter currently precludes the use of focusing optics. Instead it requires non-focusing, grid or mask-based techniques (e.g. Hurford (2013)). STIX uses Fourier-transform bigrid imaging to achieve the high angular resolution required for solar sources, an approach that is also well-suited to a limited-telemetry environment.

The imager hardware consists of two well-separated, (55 cm) x-ray opaque grids, independently mounted on the s/c Y panel (Figure **??**). Each of these grids is divided into 32 subareas with a corresponding set of 32 coarsely pixelized detectors located behind the rear grid. A pair of corresponding subareas and its detector is termed a 'subcollimator'.

Within each subcollimator the grids contain a large number of parallel, equispaced slits. The slits in the corresponding top and bottom grids windows differ slightly in pitch and/or orientation. As a result, for each window, the combined X-ray transmission of the grid pair forms a large-scale Moire pattern on the detector. The amplitude and phase of this pattern are very sensitive to the angular distribution of the incident of the X-ray flux. Thus the high-angular resolution X-ray imaging information is encoded into a set of large scale spatial distributions of counts in the detectors.

The grid design provides the imaging information in the form of a set of angular Fourier components of the source distribution (visibilities) in analogy with the imaging information provided by antenna pairs in a radio interferometer. The set of measured visibilities is then used on the ground to reconstruct an image of the X-ray source (Section 4.3.

Elements of the STIX aspect system are embedded in the center of the front and rear grids as discussed in section 4.5.)

3.3. Detector Electronics Module (DEM)

As flown, the DEM is in the form of a single Module that contains almost all the instrument active electronics. Specifically, its content and purpose include:

- 32 coarsely pixelized CdTe detectors;
- A set of 128 weak ^{133}Ba sources that illuminate the detectors with a X-ray spectrum that contains features used for energy calibration;
- Front end electronics that handle initial amplification, pulse shaping and processing of the detector output;
- An internal enclosure (Cold Unit) that thermally isolates the detectors and front end electronics. This enables enable passive cooling to maintain them at temperatures well below -15 degrees C;
- A movable Aluminum attenuator that can be inserted during high rate periods to further limit the detectors' exposure to high fluxes of low energy x-rays
- Analog to digital converters for the X-ray detectors' output
- An Instrument Digital Processing Unit (IDPU) which provides all digital processing of the X-ray data;
- Low voltage and high voltage power supplies;
- Interfaces to spacecraft power and Spacewire signals.

Power supplies, and digital electronics are duplicated and cross-strapped to provide cold redundancy.

The aspect system electronics are housed in a small module attached to the rear grid mount.

Details on the functions and implementation of the DEM are given in sections 5 and 6.

4. Imaging

In this section, we describe the imaging concept and its implementation on STIX.

As previously mentioned, the STIX imager consists of two x-ray opaque grids, separated by 55 cm. (Figure 3) As shown in (Figure), each grid is divided into 32 subareas with 30 of these 'windows' containing large numbers of equispaced, parallel slats and slits (lower panel of Figure **??**). (The remaining two grid windows serve special purposes, described in sections 4.4 and 4.4.1.) The front and rear windows are 21x18mm and 14x14 mm respectively. An x-ray detector with coarse spatial resolution is located behind each pair of windows. (Figure 1)

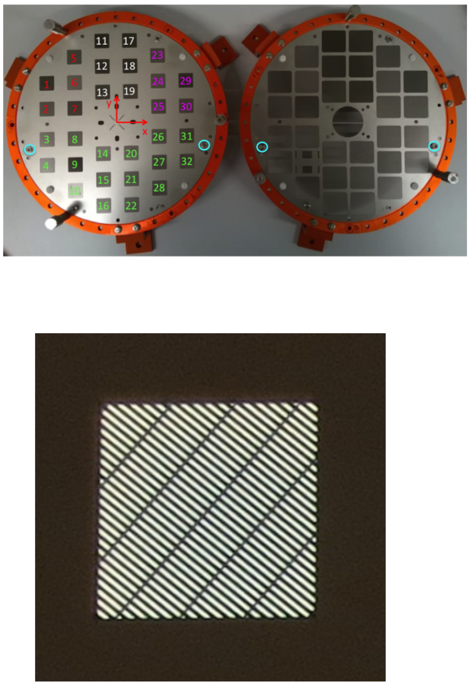

Fig. 4: (Top)Photo of STIX front (right) and rear(left) grids, mounted in their handling fixtures (red) and seen from the sun side. The blue circles indicate the locations of fiducials, used for optical characterization and grid-to-grid alignment. The numbers indicate subcollimator labels. Individual windows are 2x20 mm (front) AND 13X13 mm (rear). (Bottom) Closeup of one of the rear windows. The slats run from lower right to upper left. The five orthogonal lines are 'bridges' which add structural strength. They have no effect on imaging.

4.1. Grids

Within each subcollimator, there is a small but deliberate difference in the pitch and/or orientation of the slits in the front and rear grids. For parallel incident x-rays, this results in the combined transmission of the grid pair forming a large-scale Moire pattern on the face of the corresponding detector (Figure **??**.

The amplitude and phase of this spatial Moire pattern provides a direct measurement of a Fourier component (visibility) of the angular distribution of the source. In practice the measurement is of the Cartesian representation of the visibility (real and imagery components), which is interchangeable with the polar representation of amplitude and phase.

The grids were fabricated by Mikro Systems Inc (Charlottesville, VA) using a technique similar to that used for the fine RHESSI grids (Lin et al. (2002)). Specifically, 4 to 12 layers of 35 to 100 μm) thickness were etched and then stacked to create a grid that is effectively 400 μm) thick. [1]

---

[1] Special provisions were made in the fabrication of the 6 grids with the finest pitch 54 and 38 μ) to deal with the difficulty in etching 22 and

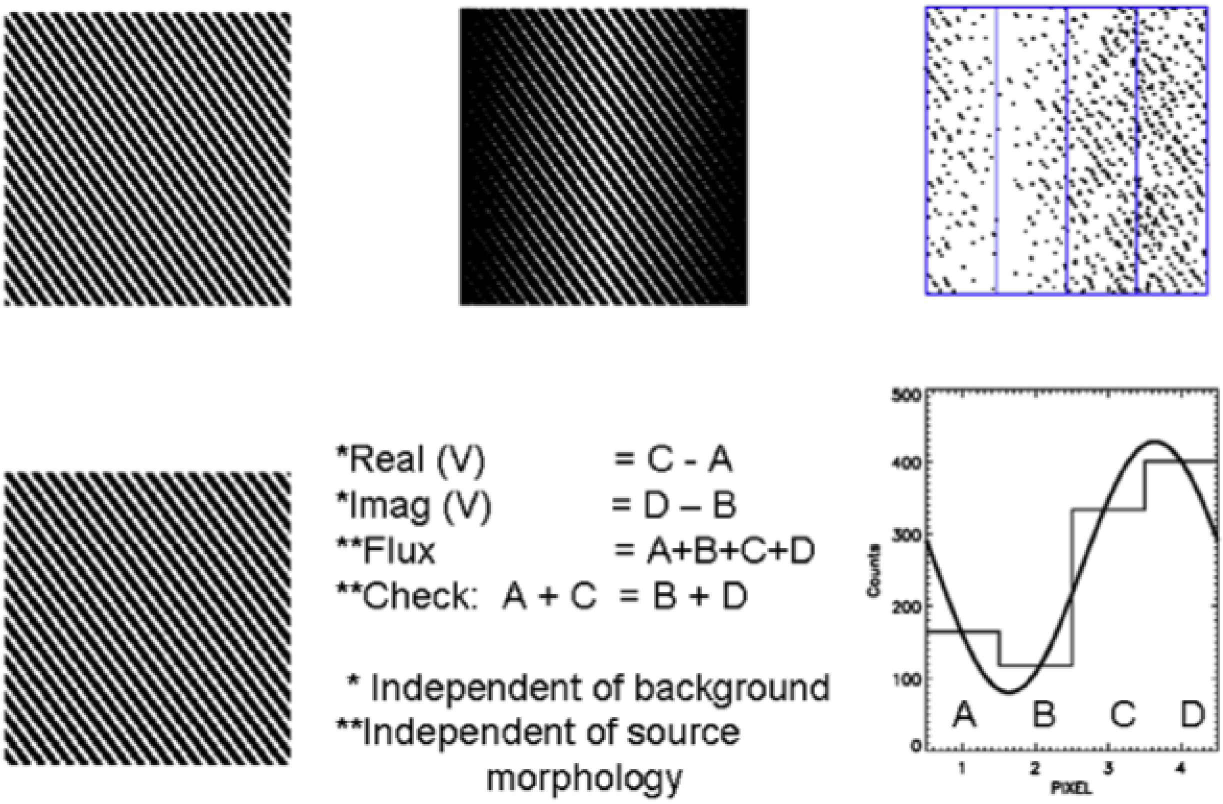

*Real (V) = C - A
*Imag (V) = D – B
**Flux = A+B+C+D
**Check: A + C = B + D

* Independent of background
**Independent of source morphology

Fig. 5: Measurement of a visibility. The left two panels show a front/rear pair of grids for one subcollimator. Close inspection shows that they have slightly different pitch and orientation. The combined transmission for an on-axis point source yields a Moire pattern (top center panel. A simulation For an off-axis source, shows the location of detected photons (top-right panel), as seen by a detector with 4 large pixels (blue). Accumulated counts in the 4 pixels are shown in the lower-right panel. Differences among these counts (bottom center) yields the real and imaginary components of the Fourier component (independent of background). The sum over the 4 pixels yields the flux (+background), independent of the visibility. There is also a cross check that is independent of the visibility.

As-built parameters of the grids were determined by 2-D optical scanning with ~ 1 μm) resolution and with ~15 keV X-rays using the Swiss Light Source at the Paul Scherrer Institute. The optical measurements were used to determine the grid pitch, orientation and phase, while X-ray imaging provided a more robust measurement of slit width.

4.2. Visibilities

The data from each subcollimator can be interpreted as a measurement of specific Fourier component of the source angular distribution. The specific Fourier frequency of this measurement depends on the *average* orientation and pitch of the slits and on the grid separation. The Fourier period is given by the ratio of the one half of th average pitch to the grid separation. (The FWHM angular resolution of a subcollimator is defined as half the period. [2]) The finest grid pitch used on STIX is 38 μm) which provides an angular resolution of (1/2 x 38 microns/550 mm) = 0.0345 milliradians or 7.1 arcseconds. In terms of orientation, the sensitivity is perpendicular to the slits. It is worth noting that with this type of imager, the complete x-ray angular response can be inferred from a set of 2-dimensional measurements of the individual grids. Direct measurement of the point-response-function of the integrated telescope is not needed.

The period and orientation of the Moire pattern is determined by the vector *difference* in spatial frequencies of the front and rear grids. For each subcollimator the difference was chosen to yield a Moire pattern with a period equal to the active width of each detector (8.8 mm) with the orientation with the Moire fringes parallel to the long axis of the detector pixels (viz. parallel to the s/c Y axis). Thus each detector sees one complete Moire period over its active area (Figure **??**).

Note that the orientation and period of the Moire pattern is a design parameter and so contains no x-ray imaging information itself. It does, however, directly measure any unexpected grid-to-grid or grid-to-detector misalignment whose effects can then be mitigated during analysis.

---

30 μm wide slits in relatively 'thick' material. For the 54 μm pitch case, the individual layers were divided into 2 'phased' subsets sets with every even slat omitted in one subset and every odd slat omitted in the other. Both subsets were then stacked together to form a grid with the correct effective pitch of 54μm but with only half the X-ray effective thickness. A similar technique was used for the finest grids with 38μ pitch, except that individual layers were etched as 3 'phased' subsets prior to being stacked. Since the slats in these grids were relatively narrow, the subareas were encased in an additional thin layer of kapton (see Figure 3).

[2] The FWHM of the point response function of synthesized beam that is formed by combining multiple visibilities depends on the relative weighting of the visibilities. This is generally broader than the resolution of the finest subcollimator. Note however, that the location of a source can be determined to much better accuracy than this resolution.

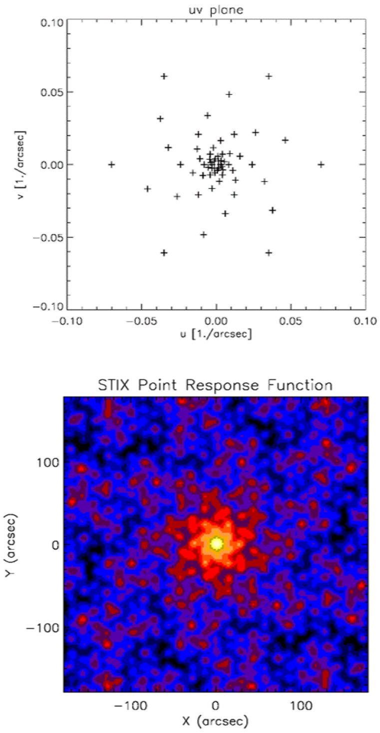

Fig. 6: (Top) Angular frequency (uv) coverage provided by the 30 Fourier components. (Bottom) Corresponding point response function, with equal (natural) weighting of all 30 visibilities, shown over a 180x180 arcsec FOV. Alternative weighting choices provide the post-facto ability to trade angular resolution for reduced side lobes in the point response function. The imaging FOV can be selected post-facto anywhere on the Sun.

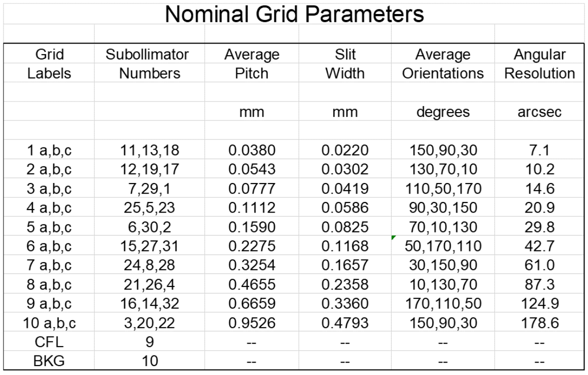
Nominal Grid Parameters

Grid Labels	Subollimator Numbers	Average Pitch	Slit Width	Average Orientations	Angular Resolution
		mm	mm	degrees	arcsec
1 a,b,c	11,13,18	0.0380	0.0220	150,90,30	7.1
2 a,b,c	12,19,17	0.0543	0.0302	130,70,10	10.2
3 a,b,c	7,29,1	0.0777	0.0419	110,50,170	14.6
4 a,b,c	25,5,23	0.1112	0.0586	90,30,150	20.9
5 a,b,c	6,30,2	0.1590	0.0825	70,10,130	29.8
6 a,b,c	15,27,31	0.2275	0.1168	50,170,110	42.7
7 a,b,c	24,8,28	0.3254	0.1657	30,150,90	61.0
8 a,b,c	21,26,4	0.4655	0.2358	10,130,70	87.3
9 a,b,c	16,14,32	0.6659	0.3360	170,110,50	124.9
10 a,b,c	3,20,22	0.9526	0.4793	150,90,30	178.6
CFL	9	--	--	--	--
BKG	10	--	--	--	--

Fig. 7: Table 2. Nominal Grid Parameters

The nominal imaging properties of the set of subcollimators is determined by the distribution of angular Fourier components that are chosen. STIX measures 10 different angular resolutions, logarithmically spaced between 7.1 and 179 arcseconds in steps of 1.43. Logarithmic spacing was chosen to provide sensitivity to a wide range of source angular sizes. At each angular frequency, there are three subcollimators with different orientations. The measured angular frequencies (uv coverage) are plotted in Figure 6 along with the corresponding point response function when these visibilities are combined. Angular frequencies and grid parameters for each of the 30 Fourier subcollimators are given in Table 2.

For a single simple source, a visibility amplitude is proportional to the total flux but also depends on the size and shape of the source. For simple sources, the ratio of its amplitude to total flux is a direct measure of its size. The visibility phase depends on the source location and/or its morphology. The choice of coarsest spatial frequency determines the maximum diffuse source size that can be imaged (~180 arcsec). Widely separated compact sources, however, can be effectively imaged regardless of their separation.

The finest spatial frequency corresponds to an angular resolution of 7.1 arcseconds. Measurements at intermediate angular frequencies provide the information needed to measure source size and shape at intermediate scales.

The measured visibilities themselves have several useful properties. For example, visibilities are linear – in two senses. Visibility amplitudes scale linearly with the incoming flux, so that visibilities corresponding to different energies and/or times can be linearly combined without introducing systematic errors. Thus, by acquiring data in relatively narrow energy and/or time bins, the analyst retains the option of combining these to enhance statistics over broader time and/or energy bins.

Viewing linearity from a second perspective, the visibility of a multi-component source is just the (complex) sum of the visibilities of its components. This property is useful for interpreting and/or anticipating the visibility of more complicated source morphologies.

Another useful property of visibilities follows from the fact that they are measured as linear combinations of count rates in different pixels. Therefore Poisson statistics in the original accumulated data can be directly converted to statistical errors in the resulting visibilities. Depending on the choice of image reconstruction algorithm, such visibility errors can then be directly interpreted in terms of statistical errors in the source properties themselves.

4.3. *Image Reconstruction*

The relationship between an image, I(x,y) and its visibilities, V(u,v) is well-known with each visibility given as:

$$V(u,v) = \int I(x,y)e^{i(ux+vy)}dxdy \tag{1}$$

where the integration is over the full angular field of view and u,v are the Cartesian components of the measured angular frequency.

With measurements of visibilities at many values of (u,v), the image can be formally reconstructed by the inverse Fourier transform:

$$I(x,y) = \int V(uv)e^{-i(ux+vy)}dudv. \tag{2}$$

Image reconstruction from a discrete set of measured visibilities is based on adaptations of well-developed techniques widely used in radio interferometry, where the direct observables are also a set of visibilities of the source angular distribution (obtained in this case from the correlated signals from separated antennas). Reconstruction techniques include back projection (which represents the convolution of the source and the point-spread-function (corresponding to a ‘dirty map’ in radio interferometry); Clean (which removes the sidelobe responses for multiple point sources), maximum entropy, Bayesian techniques, etc. The primary difference is that in x-ray imaging,

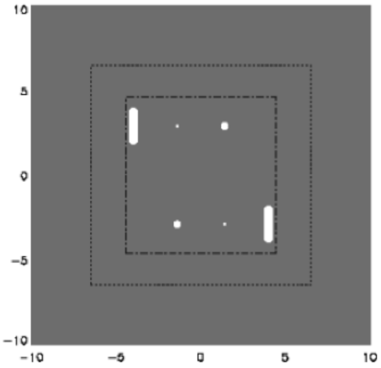

Fig. 8: Pattern of small apertures on the rear BKG grid. The aperture locations correspond to the large pixel locations on the detector.

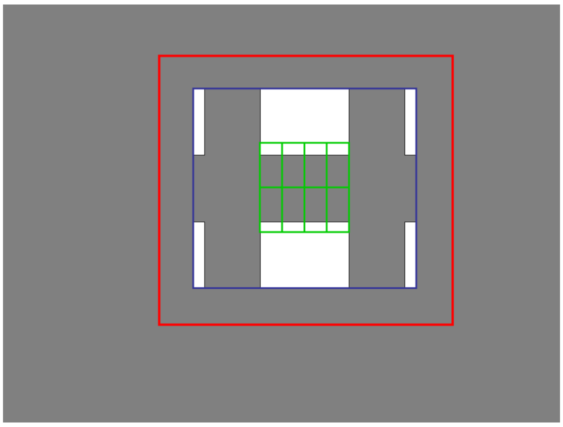

Fig. 9: Pattern of large apertures on the front grid for the CFL subcollimator. The size of the detector pixels is illustrated in green.

many fewer visibilities are available (30 in this case) compared to the hundreds or thousands typically available in radio. This limits the complexity of the x-ray source that can be effectively imaged. One measure of image quality, also used in radio, is the dynamic range which is the ratio of the intensity of the strongest to the weakest believable source in the reconstructed image. For STIX the design and calibration goal is that for a strong isolated source, a dynamic range of 20:1 can be achieved. [3]

4.4. Background Measurement

Two of the 32 subcollimators are not used to measure Fourier components. One of these, the 'BKG' subcollimator, monitors both the x-ray background and the intense unattenuated low-energy flux from large flares. The BKG subcollimator combines an open front grid window with a rear grid window that is fully opaque except for very small apertures (2 each of 0, 0.01, 0.1 and 1 mm^2) over specific large pixels (Figure 8). As needed during large flares, successive pixels in this detector can be automatically disabled. This enables the small, graduated size of the apertures to monitor both both background and incident flux while avoiding excessive count rates.

4.4.1. Coarse Flare Location

The role of the 32^{nd} subcollimator is to provide a real-time coarse, but unambiguous flare location relative to the STIX optical axis. For this 'CFL' subcollimator, the rear grid window is open and the front grid window has a coarse 'H-shaped' structure (Figure 9). Its geometry and dimensions are chosen to enable each potential flare location to provide the CFL detector with a unique pattern of pixel illumination over a 2x2 degree field of view. The On-board processing for the CFL is discussed in section 6.3.2.

4.5. Aspect

Aspect knowledge is required to compensate for potentially unstable pointing and to correctly place the reconstructed x-ray image on the sun for comparison with other images.

STIX uses the spacecraft aspect solution for roll and relative pitch-yaw aspect. This ensures the integrity of the image morphology since changes in s/c pointing during an image integration time can be fully compensated post-facto by noise-free adjustments to the visibility phases.

However, the spacecraft aspect cannot support accurate determination of the absolute position of the X-ray source on the Sun. This is because on longer (multi-week) timescales, thermo-elastic deformation of the spacecraft and/or STIX mechanical structures can change the relative direction of the STIX optical axis and the s/c reference axis. These changes must be mitigated since they are expected to exceed the goal of 4 arcsec for the uncertainty in STIX absolute source positions.

To establish the relationship between the s/c reference axis and the STIX imaging axis, a STIX aspect system (Figure 10) uses a 29 mm (effective) diameter plano-convex lens in the front grid assembly to focus an optical image of the Sun onto the rear grid. [4] Measurement of the location of the solar optical limbs on the rear grid plane then locates the STIX imaging axis with respect to the direction to Sun center. The key design feature is that the position of the critical aspect system elements (lens and solar image detector) are fixed within the grids themselves. Thus the the locations of the lens center and solar image are accurately known relative to the X-ray slits. This enables to the aspect calibration to be independent of the mechanical properties of the grid mounts and the s/c-dependent mechanical linkage between the front and rear grids.

Instead of using linear diode arrays to measure the location of the solar limbs on the rear grid, a simpler system is used which provides only the required occasional measurement of the limb location. Small (90 to 300 micron) circular apertures are etched into the rear grid, in the form of 4 orthogonal radial sets in the center of the rear grid assembly (Figure 10 inset). Behind these apertures, a set of 4 photodiodes records the integrated light passed by each set of apertures. When the solar limb passes over one of these apertures, there is a step-wise change in the output of the corresponding photodiode. Post-facto comparisons of the spacecraft aspect solution at such times establishes the offset between the STIX imaging axis (as defined by the lens center and aperture pattern) and the spacecraft aspect. Since orbital motion continually changes the apparent solar diameter, such crossings occur every few days even if the s/c pointing is stable.

The s/c aspect solution is used to monitor roll aspect. As applied to STIX, it can be calibrated by imaging cosmic x-ray

---

[3] In practice, two other factors, limited photon statistics and the source morphology, can reduce the dynamic range below this value.

[4] This lens is illuminated through an open 5 mm diameter aperture in the center of the front X-ray window. The precise aperture location does not influence the aspect calibration.

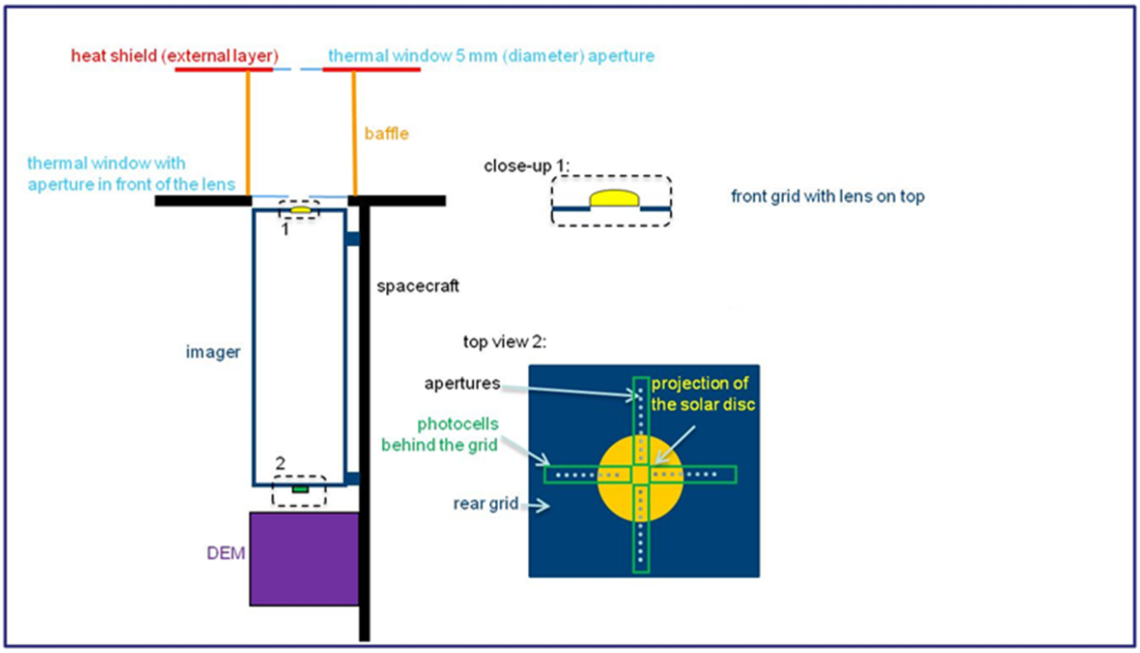

Fig. 10: Schematic view of the STIX aspect system. Viewing the Sun through a 5 mm diameter opening in the heat shield, a lens in the top grid focuses an image of the solar disk onto a set of small apertures in the rear grid plane. The response of 4 photo diodes beneath these apertures is sensitive to limbs passing over one of the apertures.) The transitions provide an occasional but accurate measurement of the location of the solar image relative to the rear grid slits.

sources (such as the Crab) when they pass within 1 degree of the sun.

5. Spectrometer and data processing unit

Expanding on the introduction in section 3.3, the following subsections describe the DEM components, starting with the enclosure and the attenuator, followed by the detectors and front-end electronics, and lastly the Instrument Data Processing Unit (IDPU) which interfaces to the spacecraft.

5.1. Enclosure

The Detector/Electronics Module (DEM) was fabricated as two separate boxes:

- A Detector Box facing the Imager that encloses the movable attenuator and a cold-unit that contains the detectors and front-end electronics;
- An Instrument Data Processing Unit (IDPU) Box behind, that contains the digital electronics and power supplies.

Joined together, they form a mechanically integrated unit that bolts directly to the s/c +Y panel.

The Detector and IDPU boxes were fabricated from Aluminum blocks as separate housings. After integrating and testing their respective contents they were combined into a single mechanical structure. Mechanically, the DEM is responsible for stable positioning of the attenuator and detectors relative to the imager; thermally, it provides the path for conductive heat transport to the spacecraft mounting panel and for supporting the thermal requirements of the *Cold Unit* inside the Detector Box.

Interconnects between the two boxes use Omnetics connectors, mounted either directly on a printed circuit board (IDPU) or on flexible Kapton extensions (Detector Box). In addition one external cable from the IDPU Box connects to the Imager Electronics Module (IEM) to support the aspect detectors and imager temperature sensors.

The Detector Box is shown in more detail in Fig. 11. Since the detectors are sensitive to humidity, the DEM has provision for a *purging system* to allow on-ground flushing with dry nitrogen to keep the relative humidity below 5%. On the front (imager side) the Detector Box is sealed with an aluminized Kapton entrance window.

5.2. Mechanical attenuator

After passing through the DEM entrance window, incident x-rays may next encounter the mechanical attenuator. When inserted, the attenuator preferentially reduces the flux of low energy x-rays (compared to high energy x-rays) to control the total count rate with minimum sacrifice of high energy counts. Its 0.6 mm thick Aluminium blades are inserted and removed autonomously into the detector field of view within two seconds, based on the decision of an on-board *Rate Control Regime* algorithm (See section 6.4). When inserted, the blades will attenuate the flux at 6 keV to 10^{-8}, at 10 keV to 2%, and at 20 keV to 60%. Attenuator operation can be disabled by telecommand.

The attenuator blades are connected to two lever arms (11) that are acted upon by two brushless Maxon motors. One motor is nominally enough to drive the mechanism, but both can operate together as a contingency. A counterweight balances the mechanism between two pivot points. Motor power is needed only to change position.

To minimize the electrical energy requirement and potential disturbances related to this, a power profile is used by which Power is increased linearly up to a first plateau, and then in-

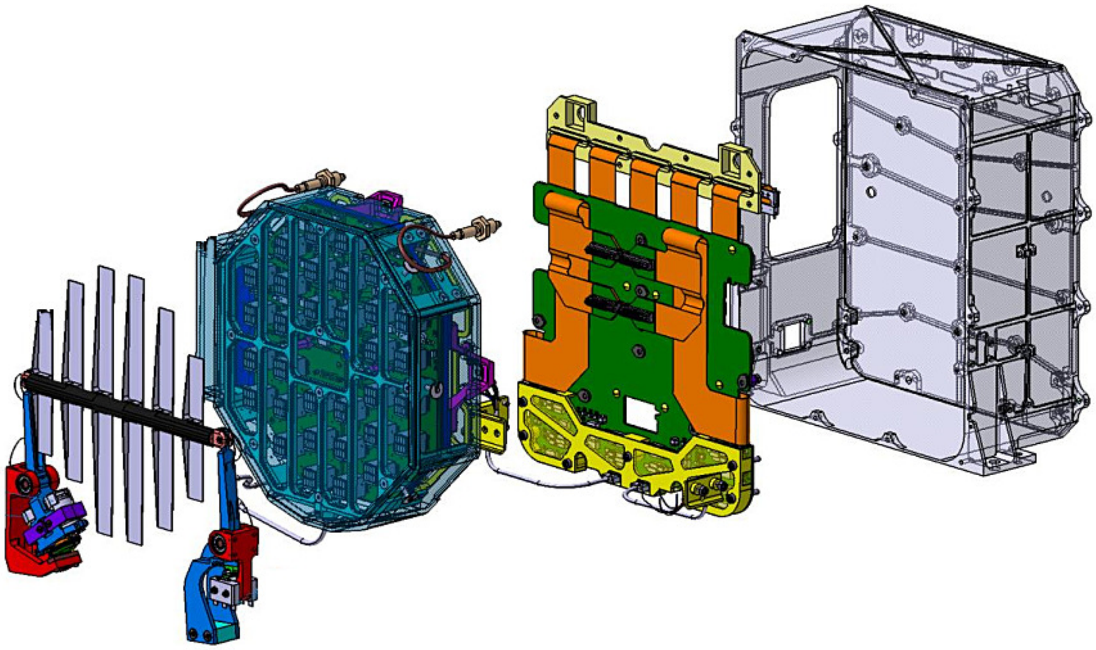

Fig. 11: Design of the Detector Box (left to right): the mechanical attenuator, the cold unit containing 32 Caliste-SO hybrids, the back-end electronics board with flex cable connections, and the housing. Not shown is the DEM entrance window to the left of the attenuator.

creased further to a second plateau. Power is switched off if either end-switches signals a successful motion, or if two seconds have elapsed since the start of the profile. The level of the two plateaus can be modified by telecommand.

5.3. X-ray detection

The combination of the energy range, high resolution resolution and low electric power budget led to the adoption of passively cooled Cadmium Telluride (CdTe) semiconductor detectors.

The STIX detector system uses an array of 32 such sensors, each 1 mm thick and 10x10 mm^2 in area.

5.3.1. Properties of Cadmium Telluride

Since CdTe has a density of 5.85 $\mathrm{g/cm}^3$ and an average atomic number of 50, it is well suited for detection of higher energy X-rays. A 1 mm thick crystal has about 65% absorption probability at 100 keV and still about 30% at 150 keV. The energy to create a charge carrier pair is 4.43 eV, yielding 870 pairs for a 4 keV photon. This underlines the requirement for a low-noise read out to obtain the target energy resolution of 1 keV full-width-half-maximum (FWHM). Low noise can only be obtained with low leakage current.

Carrier lifetimes are relatively short, typically 3 µs for electrons and 1 µs for holes in good quality CdTe that has few defects. It is thus important to collect the charges swiftly, which requires applying an electric field as large as possible. To maintain a sufficiently low leakage current despite the high voltage, the anode of the CdTe has a Schottky electrode configuration, and the sensor temperature is kept below -15°C by passive cooling through a spacecraft-provided radiator. Reverse bias in the range 200 V to 500 V is applied, much higher than would be needed for full depletion alone.

With such electric fields, the mean carrier drift length is many centimetres for electrons, but still only in the millimetre range for holes. For 1 mm thickness the electrons are therefore collected very nearly completely, but for holes the collection efficiency depends on the interaction depth. Above X-ray energies of about 50 keV, where interaction locations are distributed throughout the crystal, spectral lines consequently show a pronounced low-energy tail, as can be seen for the 81 keV line in Fig. 15.

5.3.2. Fabrication of CdTe

CdTe raw crystals of size 14×14×1 mm^3 with planar electrodes were procured from Acrorad (Japan) with a platinum cathode and gold-titanium-aluminum Schottky multi-layer anode. Patterning was done at the Paul Scherrer Institute using photolithography and a plasma etching process (Grimm (2015)). The final step is dicing to the required size of 10×10 mm^2.

The pixel pattern (Fig. 12) uses four stripes to sample the Moire pattern (Fig. **??**). Each stripe is sub-divided into 2 large pixels of 9.6 mm^2 plus a small 1.0 mm^2 pixel to help address pileup and the large dynamic range in expected count rates. Pixels can be disabled to reduce the trigger rate and dead time. This is done autonomously as part of the Rate Control Regime algorithm (See section 6.5). A guard ring around the crystal border protects the pixels from edge-related leakage current.

Selection of flight detectors was based on the following considerations:

- Manufacturer's measurements of leakage current versus bias voltage at room temperature
- Microscopic inspections before and after the patterning process.
- Pixel-by-pixel leakage current at +20°C and -20°C
- Spectroscopic performance at -20°C as measured using a ^{133}Ba source.

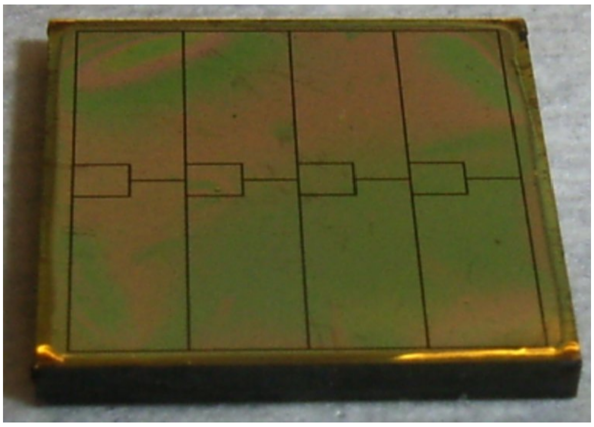

Fig. 12: View of the pixelized Schottky anode side of a STIX CdTe detector.

Fig. 13: View of a Caliste-SO with a crystal mounted on the top. The Caliste body dimensions are about 11x12x15 mm high.

To obtain energy resolution below 1 keV FWHM at -20°C, the leakage current should be below 60 pA on a large pixel at 300 V bias voltage. About 80% of all processed CdTe met this criteria. Unacceptable surface defects lowered this yield by a further 10%.

5.3.3. Caliste-SO hybrids

Each CdTe crystal was bonded to a hybrid circuit, Caliste-SO (Meuris (2012)), (Fig. 13), that contained the low-noise, low-power ASIC (IDeF-X HD described in Michalowska (2010)), plus voltage filtering and bias routing. Thirteen input channels of the ASIC are routed to pads on top of the package, interfacing with the 12 pixels and the guard ring of the CdTe crystal. (The guard ring is set to the same electrical potential as the pixels for optimum protection against edge-related leakage current.) The remaining 19 available channels of the ASIC are unused and powered off.

The trigger threshold can be adjusted individually for each channel. The signal shaping time can be adjusted for all channels combined, thus allowing a trade-off between rate capability (short shaping time) and lowest noise (intermediate shaping time). A value of about 5 µs provides the lowest noise for STIX. The noise is also affected by the capacity of the pixels, resulting in better energy resolution for the small pixels (Fig. 15).

5.3.4. Front-end electronics

The Caliste-SO are accurately positioned and mounted on front-end electronics boards. To minimize power dissipation near the crystals, these boards contain only minimum support circuitry, high-voltage voltage filtering and distribution components. Other components such as the ADCs, regulators and test pulse circuits, are mounted on a back-end board outside of the cold unit (Fig. 11). Kapton cables with low heat conductivity are used for interconnection between front-end and back-end. To further minimize thermal leakage through control cables, each ADC services two detectors, The detector pairs are chosen so that the loss of a single ADC results in a minimum impact on imaging.

For redundancy, the front-end is electrically divided into four identical quarters. Two high-voltage channels are used, each supplying two quarters. As with the grid pairs, the relation between quarters and grid parameters was chosen to minimize the impact of the loss of any single quarter or of a single HV supply.

The total processing time for a trigger is about 12.5 µs. This time is the same even if more than one pixel (in a detector pair) is triggered. Since the interpretation of such multiple-hit events can be ambiguous, they are subsequently discarded. A single readout is still performed, however, to guarantee that the contribution to the dead time remains the same.

5.3.5. Cold unit

The cold unit (see Fig. 14) is a thermally isolated enclosure within which are the detectors, Caliste and other front-end electronics. Passive cooling is used to maintain the interior temperature and is accomplished via a STIX-dedicated radiator thermally connected to the aluminum-beryllium alloy cold plate inside the cold unit. A temperature of -25°C can be maintained at the interface to the spacecraft provided the heat load does not exceed 3.2 W.

The inside of the spacecraft and the DEM housing will be warm during observation times near perihelion (the worst-case design temperature is +50°C), therefore the cold unit requires excellent thermal insulation. The circuit board with the Caliste-SO hybrids is mounted on the cold plate, which is insulated by Vetronite elements and multi-layer insulation (MLI). The cold unit meets the 3.2 W heat load requirement with a single-piece MLI design that combines 1.2 W to be generated electrically by the front-end electronics, plus leakage of 1 W each for conduction and radiation.

The cold unit design must also ensure that the x-ray transmission through the MLI is uniform across the front face. Otherwise false visibility signatures would be apparent in the spatial distribution of the detected x-rays. Calculations based on the material structure and measured at 5.9 keV found the design to be compatible with the 4% rms the requirement for transmission homogeneity at 6 keV.

5.4. Energy calibration Sources

Imaging in a given energy range is based on the relative count rates among different detectors and pixels. In the presence of steep flare spectra, the count rate ratios (and hence the imaging) would be potentially compromised if the relative energy calibration were not accurately known (goal: 100 eV rms). The goal is addressed by continuously illuminating each pixel with x-rays from ^{133}Ba radioactive sources inside the cold unit. For each pixel, ground analysis of the resulting spectra determines

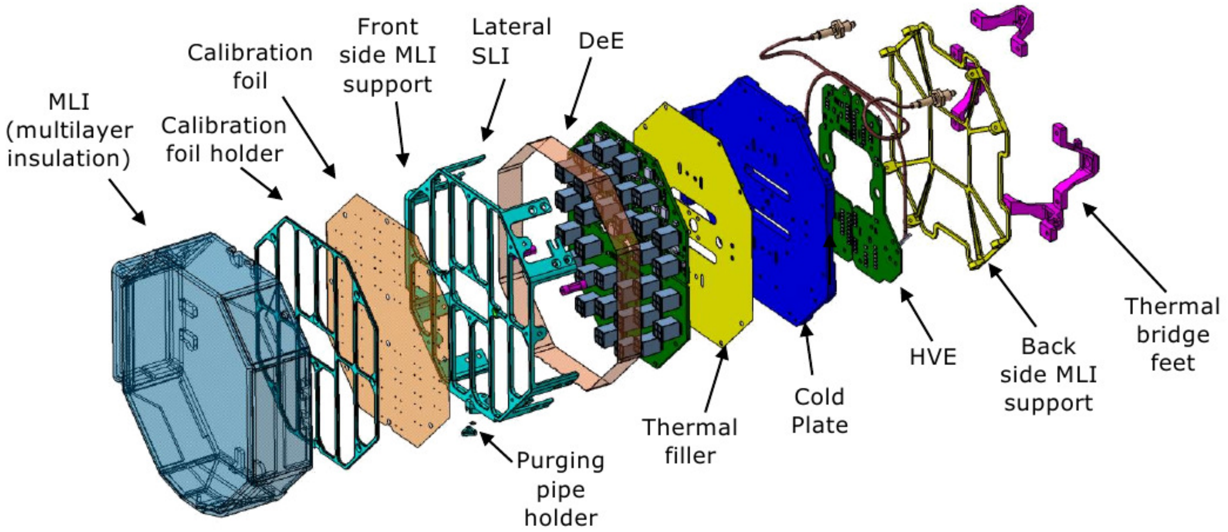

Fig. 14: Exploded view of the cold unit. The cold plate (blue) is connected to the spacecraft radiator, the front-end electronics is mounted on this plate. This is enclosed by multi-layer insulation and supported by Vetronite thermal bridge feet (pink).

the ADC channels corresponding to two peaks of known energy. The results are then uploaded to STIX for real-time application. (See section 7.2.1)

The source activity that is necessary to obtain such a calibration should be sufficient to overcome background while not unduly degrading the instrument sensitivity to weak flares. Pre-launch estimates of the background were based on Geant4 Monte-Carlo studies which indicated that the background will probably be dominated by direct observation of the well-known diffuse cosmic x-rays, with a smaller contribution from partially-shielded time-variable charged particles. This led to the selection of a total source activity of 4.5 kBq, distributed over 128 individual dots to ensure comparable illumination of all pixels.

Ground tests confirmed the feasibility of this process using spectral measurements with the internal calibration source in the fully assembled DEM during the final thermal-vacuum testing campaign of STIX. Results from this test are shown in Fig. 15.

5.5. Sensor degradation

5.5.1. Polarization effects

Schottky CdTe detectors are subject to a *polarization effect*, a change of the internal electric field as function of time under bias due to varying space charge Cola (2009). In general this results in a leakage current increasing with time, decreasing resolution and reduction of the sensitive volume. The sensor can be restored to the pre-polarized state by a relatively brief removal of the applied bias. Measurements at a temperature of +4°C and 200 V bias indicate a typical time scale of about half a day for doubling the FWHM. Setting the bias to 0 V for two minutes completely restored the initial performance. The polarization interval increases with decreasing temperature and is about one month at the nominal operating temperature of -20°C. Short bias resets on a daily time scale are foreseen to be executed automatically in flight. The reduction in livetime due to this effect is thus negligible.

CdTe is also subject to a rate-dependent polarization effect. However, this sets in at rates in the range (1-10) $\times 10^6$ $/(mm^2 s)$, and so may only become relevant for low-energy spatially-integrated spectroscopy using the (unattenuated) BKG detector during events that exceed GOES $\sim X10$.

5.5.2. Radiation damage to detectors

Many different components on the spacecraft and payload will suffer radiation damage during the 10-year mission. Of particular importance to STIX is the degradation of its CdTe sensors. This is due to displacement damage in the crystal lattice from non-ionizing energy loss of energetic protons (Eisen (2002)). The dominant source of this degradation is the episodic short-lived high fluences of those particles during *solar proton events*, as opposed to the continuous exposure to galactic cosmic rays. [5]

To estimate the degradation that has to be expected, CdTe crystals from the production were irradiated by 50 MeV protons with a fluence of $1.6 \cdot 10^{11}$ cm^{-2} at the Proton Irradiation Facility of the Paul Scherrer Institute. This results in about the same non-ionizing energy deposition than the actual proton spectrum. The range of protons with this energy in CdTe is 6.7 mm, so an approximately homogeneous damage distribution is obtained in the 1 mm thick material.[6] In the test, the total fluence was accumulated over a period of 20 hours with a flux of $2.2 \cdot 10^6$ s^{-1}cm^{-2}. Ten unbiased CdTe crystals were irradiated at room temperature[7]. To obtain degradation data as a function of exposure, two detectors were removed after each 20% fluence step.

After about one week, the crystals were evaluated for leakage current and spectral performance (energy calibration and resolution). The observed evolution with fluence of the FWHM at 31 keV and of the energy calibration offset is shown in Figure 16. The behaviour of the resolution at 81 keV was similar to the low energy line, rising roughly linearly to an average of 12 keV at

---

[5] See section 4 of TEC-EES-03-034/JS, *Solar Orbiter Environmental Specification*, Issue 3R1 (13 June 2012), for the expected mission-integrated proton fluence spectrum.

[6] The neutron fluence at the location of the CdTe crystals was estimated through a Geant4 simulation to be negligibly small.

[7] In flight the detectors will be constantly cooled, but biased only during allocated observation windows. There are no indications, however, that the results would be significantly changed depending on bias or temperature.

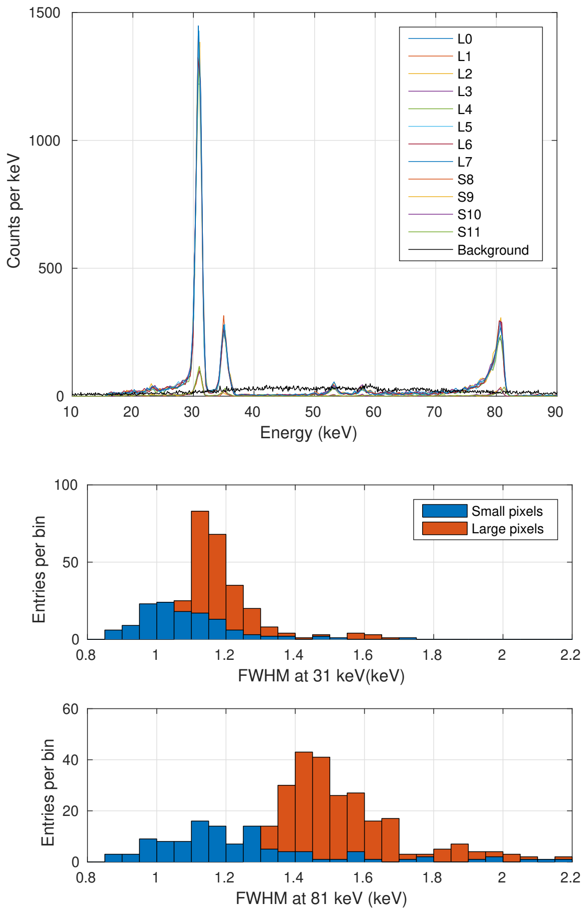

Fig. 15: (Top) Energy spectrum obtained with the ^{133}Ba internal calibration source for sub- ID 5 (top). The count rate was 87 s^{-1}. The expected background in flight for a large pixel is also shown. Full-width-half-maximum energy resolution for all 384 pixels at 31 keV (middle) and 81 keV (bottom). The better energy resolution of the small pixels can be clearly seen in the figure, resulting mainly from their smaller capacitance. At the shorter shaping time of 1.78 µs, the resolution is worse by about 200 eV.

100% fluence, with a large spread among pixels. In practice, a continuous change in the in-flight spectral performance and energy calibration is partly mitigated since the calibration and resolution are monitored on-board with a radioactive source so that the analysis and FSW parameters can be updated accordingly. Retests of the irradiated crystals after 3 months storage at room temperature showed that annealing would not be sufficiently beneficial to be useful in the Solar Orbiter context.

5.6. Instrument Data Processing Unit

Direct digital control of STIX components is via a single FPGA with a 100 MHz main clock, located in the IDPU (Instrument Data Processing Unit). It connects to the front-end and back-end electronics, the power supplies, acquires house keeping data, interfaces with various memories and with the spacecraft via SpaceWire.

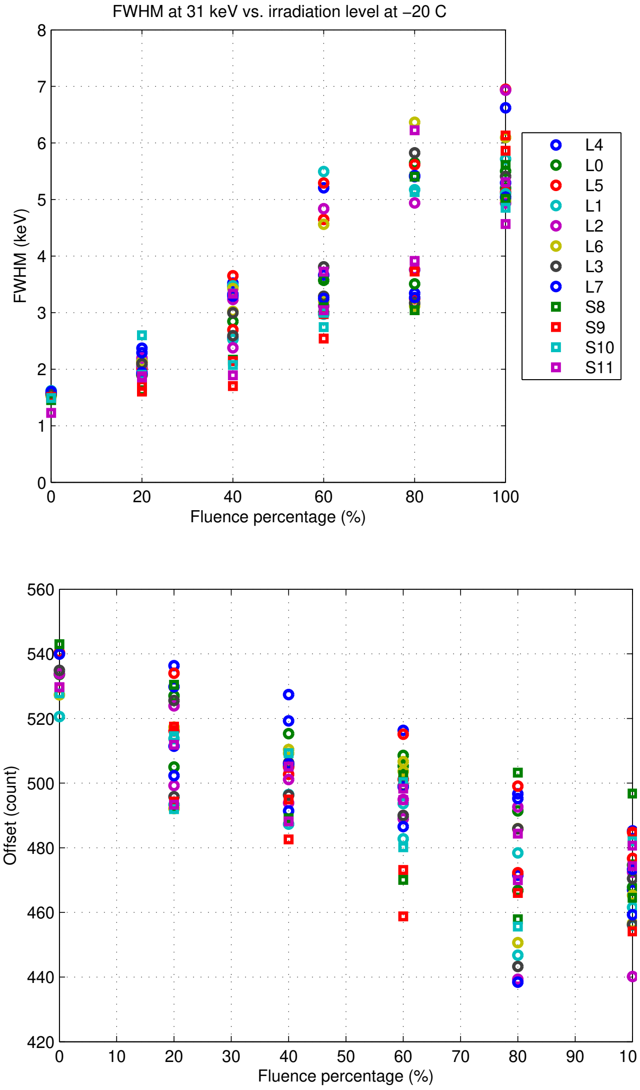

Fig. 16: Two results from the proton irradiation studies. The evolution of the FWHM at 31 keV (top) and the energy calibration offset (bottom) are shown for all 12 pixels as a function of fluence for the the 8 large(L) and 4 small(S) pixels. One year in flight corresponds on average to about 10% fluence.

Two nearly identical boards containing the main IDPU components are available in cold redundancy.[8] A switch-board interconnects the two boards and interfaces to the front-end, the Imager electronics, and the Power Supply Unit (PSU).

The flight software runs on a LEON3 Sparc3-type processor with 20 MHz clock frequency, synthesized on the FPGA. The software is divided into two separate parts: the immutable start-up software (SuSW) and the modifiable application software (ASW). Upon application of power to the IDPU, the SuSW is executed automatically. It performs basic power-on health checks and provides boot telemetry to the spacecraft. If no blocking issues are detected, it loads the ASW from Flash memory and transfers control to it. The SuSW also provides the capability to upload new versions of the ASW from ground, either in full or by patching.

---

[8] The difference between the boards is an identification accessible to the FPGA, indicating if the currently running board is the main or redundant one.

The ASW contains all control and science functionality. Its organization and functions are described in section 6.

5.7. Power supply unit

The spacecraft provides the PSU with two +28 V lines, one for the main and one for the redundant side (cold redundancy). Commands to the spacecraft select which side of STIX is used. The PSU contains the circuitry for handling the spacecraft HPC High Power Pulse Command (HPC) signal and Bi-level Switch Monitor (BSM) read-back.

All low voltages are generated via windings on a single, main transformer, then regulated and filtered as required. Analog voltage, current, and temperature measurements are passed to the IDPU for digitization. The PSU also contains two high-voltage DC-DC converters to supply the CdTe sensors via the front-end electronics, each converter supplying one half of the sensors without cross-strapping. Both converters are accessible by the main and the redundant side.

The low voltages are divided into essential and non-essential lines. The essential voltages comprise the FPGA and SpaceWire lines, which cannot be switched by STIX itself. In case a severe anomaly is detected on them, a telemetry report will be send to the spacecraft, requesting an immediate power down. The non-essential lines supply the detector front-end, the aspect system, the attenuator, and the high-voltage supplies. They are switched under software control, and will be disabled in case an anomaly results in a transition to safe mode.

6. Onboard Data Handling

This section describes the on-board handling of the digitized x-ray and aspect data.

The design driver for the IDPU's x-ray data processing is the need to reconcile an input stream of up to 800,000 photons per second ($\sim$ 20 Mbits/sec) to a telemetry budget of 700 bits per second. This is done by combining rapid FPGA sorting and accumulation of individual events with slower application software that processes the accumulator contents. Figure 17 indicates the overall data flow.

The goal of the FPGA's prompt processing is to sort and sum the input photon stream into accumulators on the basis of their detector ID, pixel ID and detected energy *in keV.* Application software running on a LEON3 processor then proceeds along three parallel paths:

- a primary path that handles the x-ray imaging and spectroscopy data;
- a quick-look (QL) path that supports the generation of light curves and other products used to monitor the performance of the instrument and to provide a continuous overview of solar activity;
- an energy-calibration path that acquires data needed to establish the energy calibration of each detector/pixel.

6.1. Prompt processing

From a digital perspective, the x-ray input to this task consists of an asynchronous stream of 24-bit 'photon words', each of which corresponds to a single detected x-ray, specified by the detector ID (5 bits), pixel ID (4 bits) 3 spare bits and the 12-bit ADC output which is a linear representation of the detected photon energy.

The first step in handling each photon word is to correct the ADC output for a known weak temperature dependence. This correction is implemented by applying a small detector-, pixel- and temperature-dependent offset (configurable) to the 12-bit ADC output for each photon. The modified ADC values are used for subsequent processing where they can be considered to correspond to a common, predetermined reference temperature.

Since it is neither practical nor necessary for the primary and QL paths to retain the full 12-bit energy resolution, the next processing step is to rebin the detected energy for each photon into one of 32 broader 'science energy channels'. This is done by the FPGA with a detector- and pixel-dependent, programmable look-up table. The rebinned energy provides 30 energy channels between 4 and 150 keV plus two integral channels for energies above and below these limits. An important rebinning feature is that despite potentially different calibrations, the boundaries that separate the science energy bins are matched in terms of keV among all detectors and pixels. Also, rather than having equal widths, the science energy bin widths are optimized for typical flare energy spectra, typically with a 1 keV width at lower energies, broadening gradually at higher energies. Simulations have shown that energy binning on this scale does not degrade spectroscopic analyses.

6.2. Primary data path

In the primary data path, each photon word increments one of 12288 double-buffered accumulators (32 energies x 32 detectors x 12 pixels). Accumulation continues for an integral number of 0.1s periods until one of 2 conditions is met: 1) a preset minimum integration time has been exceeded AND a preset count threshold (within a specified energy range) has also been exceeded; OR 2) a preset maximum integration time is reached. The use of programmable, adaptive integration times enables subsequent data handling to be efficient during solar quiet periods while still supporting high time-resolution as needed during flares. With suitable parameter selection, the option of fixed integration times is still available.

As each integration is completed, the FPGA transfers the contents of the accumulators into a time-tagged rotating buffer. The contents of the rotating buffer are subsequently compacted (partly by eliminating accumulators with zero counts) and stored into 16 GBytes of flash memory. This 'archive buffer' can be retained on-board for several weeks and provides the input for all subsequent primary analyses. It is important to note that despite the foregoing energy and time binning, the archived data can be considered scientifically lossless in the sense that higher time- or energy-resolution could not be exploited for statistically significant solar analysis.

In parallel with the photon word handling, one of 16 trigger counters is incremented each time an event is seen by a 'not-busy' detector. Trigger counters accumulate for the same time intervals as the event counters and their output is carried along with photon counts in subsequent data handling and analysis steps. Photons that are detected in more than one pixel in a detector pair generate a single trigger but are otherwise excluded from subsequent analysis and do not generate a photon event word. The dead time is digitally the same for all triggers (nominally 12.5 microseconds). Therefore the trigger rate alone is sufficient to directly measure the live time for the corresponding detector pair. An important corollary is that all pixels in a single detector share a common live time. This greatly eases the interpretation of count rate ratios which form the basis for imaging.

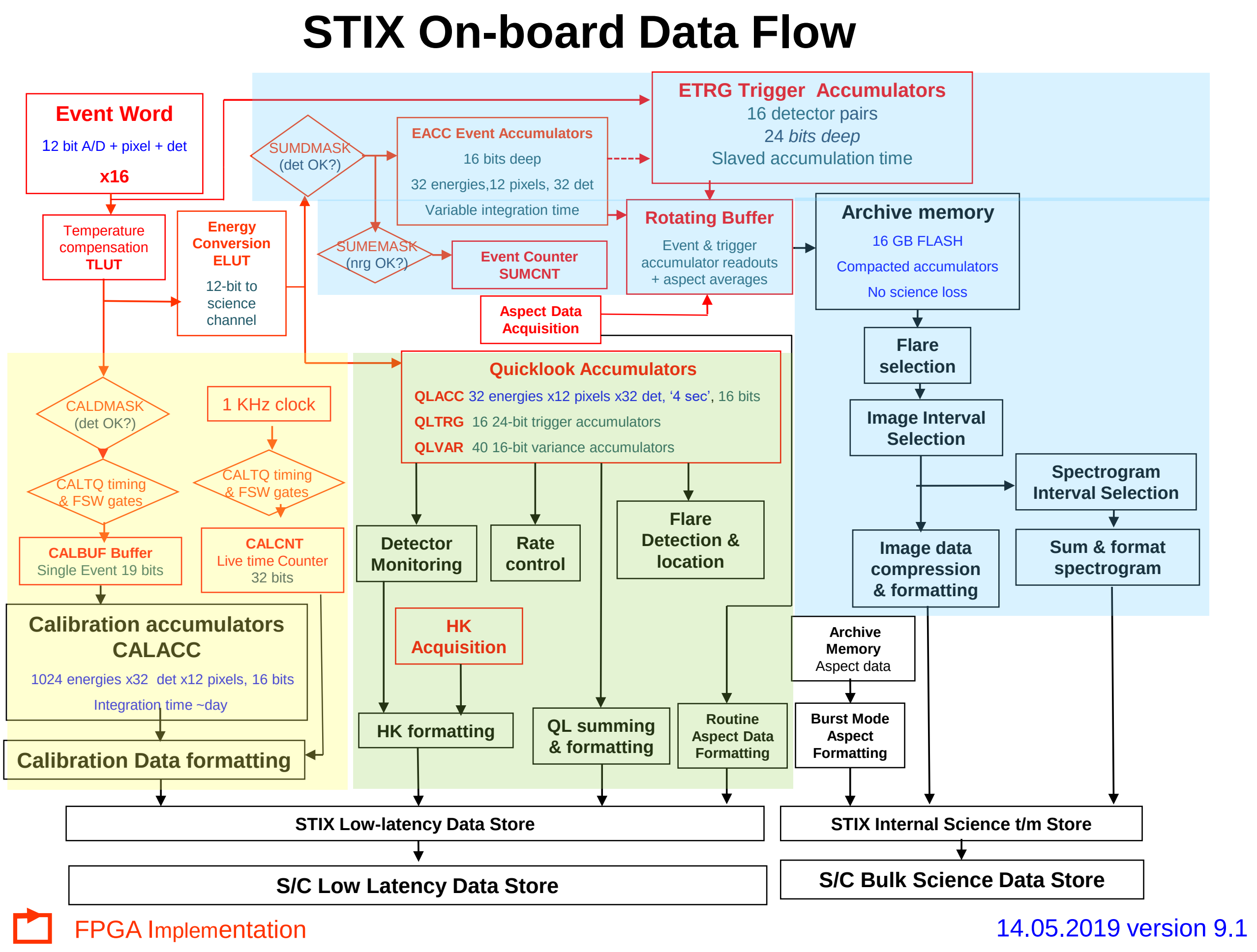

Fig. 17: Overview of the on-board data flow. Red boxes indicate FPGA processing; Blue background is primary data path; Green is the QL data path; Yellow is calibration data path.

6.3. Quick-look data path

As with the primary data path, the QL data path also begins by feeding the photon words into a (separate) set of 12288 double-buffered accumulators. In this case, the accumulation intervals are fixed (4s nominal). Except as noted below, the calculation of QL products must be completed within the 4s QL integration time. In most cases the calculation QL values requires only summing various combinations of the QL accumulator contents, in four cases, (Table 18 more extensive calculations are required. These are discussed below.

6.3.1. Flare detection

The goal here is to detect flares in real time and to provide a rough measure of their intensity. The detection algorithm uses two time sequences of detector-summed counts, corresponding to different energy bands (to support detection of thermal and nonthermal x-rays). For each band, two different averaging times (multi-second and multi-minute) are used to provide sensitivity to both impulsive and gradual events. A flare is deemed detected when current counts in any of the 4 cases exceeds a preset minimum count rate while representing a significant fractional increase relative to a longer term average. The flare is deemed to have ended when all the triggering count rate(s) fall below a preset fraction of its maximum. The flare status is included in real-time data transmitted to other instruments with an overall 4 to 8 second latency.

6.3.2. Coarse flare location

As discussed in section SECT:CFL, the CFL subcollimator illuminates its detector with a unique pattern that depends on the flare centroid location relative to the STIX imaging axis. Combining the 8 CFL pixel count rates with averages from other detectors, the centroid location is estimated onboard (in successive 8-second nominal intervals) by maximizing the correlation of the various count rates with expectations calculated for an array of 65x65 potential flare locations. The result is digitized to 2 arcminutes and included in the data distributed to other instruments in real time.

To ensure adequate statistics while avoiding potential nonlinear effects at very high count rates, the real-time flare location is calculated only when flare count rates are at intermediate levels. This should not be an issue since once underway, flare centroid locations are relatively stable on a 2-arcminute scale.

6.3.3. Detector monitoring

The purpose of this task is to identify malfunctioning detectors that exhibit abnormally high count rates. Although such detectors can increase the volume of t/m and data within the archive

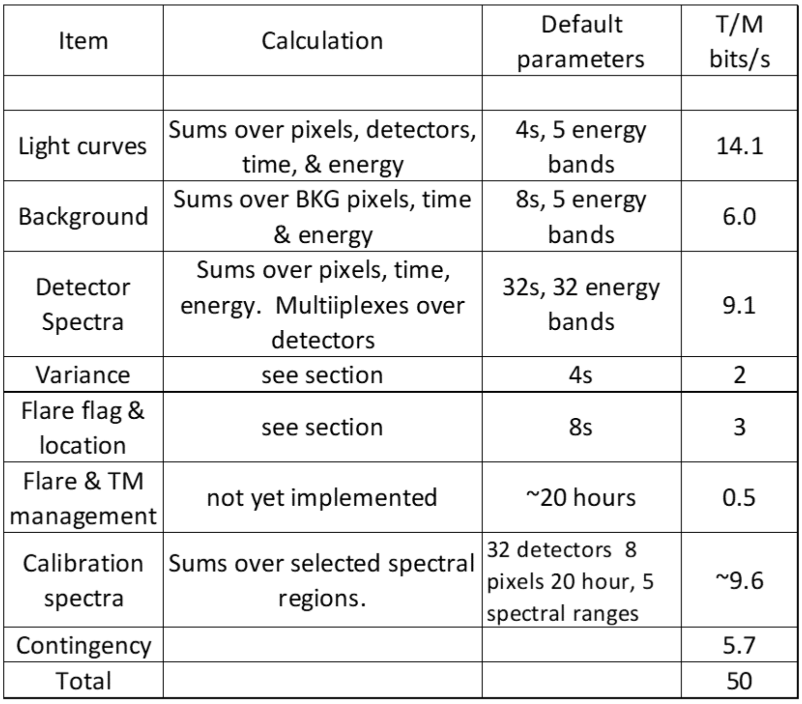

Item	Calculation	Default parameters	T/M bits/s
Light curves	Sums over pixels, detectors, time, & energy	4s, 5 energy bands	14.1
Background	Sums over BKG pixels, time & energy	8s, 5 energy bands	6.0
Detector Spectra	Sums over pixels, time, energy. Multiiplexes over detectors	32s, 32 energy bands	9.1
Variance	see section	4s	2
Flare flag & location	see section	8s	3
Flare & TM management	not yet implemented	~20 hours	0.5
Calibration spectra	Sums over selected spectral regions.	32 detectors 8 pixels 20 hour, 5 spectral ranges	~9.6
Contingency			5.7
Total			50

Fig. 18: Calculation of Quick Look T/m items

buffer, their most serious impacts are that they may provide erroneous input to the QL light curves and to some on-board decision-making algorithms. Restricted to non-flaring times, the detector monitoring task identifies any detector with count rates that persist at significantly higher levels than those of its peers in either of two preset energy ranges. The offending detector is then flagged in appropriate masks to exclude it from an decision making role and QL light curves calculations. More detailed diagnostics, mitigation and restoration are handled after the fact by the ground segment.

The on-board impact of detectors that fail by not providing any output at all is much more benign and so their identification and mitigation is deferred to the ground segment.

6.3.4. Rate control regimes

This task uses detector-summed trigger rates to make decisions as to the most appropriate attenuator and pixel states to maintain viable event rates without necessarily sacrificing sensitivity. Details are described in section 6.5.

6.3.5. Variance calculation

To monitor for either 'bursty' detectors or significant subsecond time variations in the solar flare flux. a variance measure is calculated and included in the QL data. This is achieved by accumulating detector-summed counts in a preset energy range into a set of 40 successive 0.1s time bins. After 4s has elapsed, a variance measure among the contents of these 40 accumulators is calculated and transmitted as part of the QL t/m. The noise-free conversion to actual variance and evaluation of its statistical significance (if any) is done on the ground.

6.4. Calibration Data Path

The purpose of the calibration data path is to obtain high resolution spectral data from the weak on-board ^{133}Ba x-ray source (see section xx). This data provides the input to ground-based spectral fits that determine the gain and offset for each detector and pixel. The on-board spectral accumulation is based on a 10 bit representation of the 12-bit (temperature-compensated) ADC output in the event word. Events are summed into 393216 accumulators (1024 energies x 32 detectors x 12 pixels) over a commandable multi-hour timescale. To ensure that the ^{133}Ba spectra are not overwhelmed by solar photons, accumulation is restricted to periods when the Sun is quiet. This determination is made by requiring that no event be accumulated unless a specified time interval ($\sim$ *milliseconds*) has elapsed since a previous photon detection. Such a criterion automatically suppresses accumulation during periods of enhanced solar count rates. To establish the normalization of the resulting spectra, live time is measured using a 1 kHz oscillator whose output is gated and summed over the same times as when an incoming event could be accumulated.

After the x-ray accumulation is ended, the resulting spectra can be flexibly truncated and/or averaged and the results included in the telemetry as QL data.

6.5. High rate handling

STIX is exposed to solar photon fluxes that can range from background levels of $\sim 10^2$/events/s to over $\sim 10^{10}$ photons/s for flares above GOES X10. Such a range implies that the detector and data handling limits of $\sim$800,000 /s can be exceeded. Several strategies, outlined below, are applied successively to avoid exceeding the count rate limits.

- Individual detectors can analyze up to $\sim$20,000 events/s by relying on live time measurements (up to $\sim$50%) to renormalize the observed count rate data. This supports the basic capability of ~800,000 /s.

- At potentially higher count rate levels the movable aluminum attenuator (see section 5.2) can be inserted in front of the detectors to reduce the intense low-energy photon rate from flares by a factor of 10^2 while still transmitting almost all the high energy photons. Renormalization as a function of energy is performed during post-analysis.
- At still higher levels, individual pixels can be temporarily disabled (e.g. top and/or bottom rows of large pixels) to reduce the effective detector area (and count rates) in 3 successive steps by up to a further factor of 20.
- An additional option ('pixel cycling') is available that cyclically enables selected individual pixels or pixel pairs on a short timescale so that only one or two pixels in each detector are active at any one time. While still rapidly sampling the complete Moire pattern. this provides up to a factor of 4 reduction in instantaneous rates, adding additional dynamic range.

Overall the combination of attenuator insertion, pixel disabling and pixel-cycling can reduce the rate of analyzed events by up to a factor of $\sim 10^4$. In practice, taken together, these strategies result in up to 8 specific instrument configurations or "rate control regimes" (RCRs) that are invoked and relaxed sequentially under software control. There is a latency of 4 to 12 seconds between the occurrence of an enhanced rate and its mitigation by changing the RCR.

6.6. Autonomy and data selection

As the foregoing discussion suggests, there are three important distinctions between the QL and primary x-ray data handling: the first is that the QL data do not deal with imaging; the second is that the QL data are acquired and transmitted with fixed parameters such as a 4s cadence; third, there is no QL provision for on-board data selection. In contrast, the much more voluminous primary data can only be transmitted on a highly selective (flare-associated) basis albeit with a wide range of choices for time and energy resolution and coverage. These choices can be optimized to match the dynamic characteristics of the flare in question. Thus by limiting consideration to flare intervals only, and by optimizing time and energy range and resolution for the individual flare, the scientific efficiency of imaging and spectroscopic data telemetry can be greatly enhanced.

There are two approaches to selecting the time- and energy-resolution and range of the spectroscopic and imaging data. The first approach relies on the ground segment to select parameters for the downlink of flare T/M. This selection can be based on the QL light curves in 5 different energy bands which together provide a robust indication of flare timing, intensity and spectral properties. The ground segment can use this to choose optimized time and energy range and resolution for different phases of the flare, predict the resulting TM volume and upload corresponding analysis requests. The onboard software then applies these parameters to the data stored in the archive buffer. This option is viable because the latency of the QL data (24 to 48 hours) is much shorter than the multi-week longevity of the archive buffer. This provides time for the ground segment to make selections and upload parameters and for the FSW to process the data. However, there are two downsides to this approach. The first is that the selections and choices must be made before the on-board archive is overwritten and so cannot be deferred indefinitely; the second it that there is an operational latency of at least a few days between flare occurrence and the transmission of the requested x-ray imaging and spectroscopic data.

With the second approach ('autonomy'), the FSW uses the output of the on-board flare detection algorithm to identify relevant time ranges. It then uses automatic, parametrized algorithms to optimize the time and energy resolution for imaging and spectroscopic data for inclusion in bulk T/M. As of this writing, this option has not yet been fully implemented.

For preparing the telemetry, the data for each specified time/energy bin (termed one 'image') is compressed to one of four user-chosen data compression (DC) levels. The different DC levels provide the ability to tradeoff telemetry volume for redundancy in the downloaded bulk science data. (Except for the self-calibration and data volume, the choice has no direct effect on image quality.) The four available options are:

- Data Compression Level 0: This data compression level downlinks the raw unaveraged counts within a specified time interval in the archive buffer. This is very inefficient and should be used only for diagnostics.
- Data Compression Level 1: For each specified pixel and detector, counts are summed within each requested time/energy bin. This data set retains the full inherent redundancy which can be used for self-calibration. For perspective, with DC Level 1 compression, the STIX baseline t/m allocation is sufficient to transmit up to $\sim 10^3$ user-specified images per hour, each corresponding to a well-defined time/energy bin.
- Data Compression Level 2: This is the same as DC level 1, except that instead of individual pixels, counts are also summed over specified pixel combinations. This can save up to ~50% of the T/M compared to level 1, but discards much of the self-calibration information and precludes some types of instrument response corrections.
- Data Compression Level 3: For each time/energy bin, specified combination of pixels and detectors, counts are summed and/or differenced for inclusion in T/M. The resulting T/M can be interpreted directly in terms of visibilities. This saves an additional ~20% of T/M. However, it contains relatively little information that can be used for self-calibration.

No image reconstruction is done on board. Instead, for any of these compression options, the detector data for a time/energy interval can be used to calculate a set of calibrated visibilities. Ground-based image reconstruction then yields a corresponding image. Such images can be interpreted directly, combined to form a temporal 'movie' or to obtain feature-dependent spectra. Additional insights can be obtained from time, detector and spectral comparisons of the amplitude and/or phase of the visibilities themselves.

As with imaging data, users can also specify time/energy range and resolution for spatially-summed flare spectroscopy data. Since the data volume is relatively modest, finer time/energy bins can be chosen and only one option for data compression is needed. In this case an individual datum corresponding to detector- and pixel-summed counts within the specified time/energy bin. For organizationaland implementation purposes this can be considered as DC level 4.

6.6.1. Aspect Data Handling

Aspect data are included in the telemetry in two forms: First, regular aspect is included in the Housekeeping telemetry on a quasi-continuous basis at low (64 s) time resolution, a cadence that is suitable for periods of stable pointing. Burst mode aspect is included in bulk science telemetry only upon post-facto request by the ground segment which specifies the time interval and cadence (1/64 s to 32 s). This option is intended to provide high rate aspect data for periods when the pointing is varying. The aspect data to support post-facto burst mode aspect selections is stored as part of the archive buffer with a longevity similar to the x-ray data.

To generate aspect data, the analog output of each photodiode is digitized by a multiplexed 12-bit A/D converter running at 1024 Hz. For each photodiode, 16 successive outputs are summed into a 16-bit word at a 64 Hz rate. These words are stored in the archive buffer from where it provides the input for optional post-facto burst mode aspect telemetry.

In parallel, the 64 Hz stream of aspect values are sampled every 4 seconds. For each photodiode, 16 such samples are averaged every 64 seconds and the averages included in the housekeeping telemetry. This regular aspect data requires about 1 bit per second of telemetry.

6.6.2. Integer compression

In addition to the foregoing, all individual values for x-ray count and trigger sums in the QL and bulk science T/M are compressed to 8 bits from their multi-byte internal representations. This integer compression uses a quasi-floating-point format (with parametrization appropriate for each data type) whose range can accommodate maximum realistic expectations. Low values are represented exactly; compression errors for larger values correspond to a fixed fraction ($\sim$ 1.5 to $\sim$ 3% rms) of the uncompressed value. Ground decompression is based on lookup tables. Except for x-ray and trigger telemetry values, integer compression is not invoked for any other on-board data handling. In some cases, the use of compression should be considered in evaluating the statistical significance of results.

7. Operations, Data Products and Analysis

This section provides an introduction to STIX instrument operations, calibration, data products and science analysis, including the interactions among STIX flight hardware, flight software and the ground segment.

7.1. Operations

The STIX instrument has provision for 6 operating modes:

- OFF: Totally unpowered
- BOOT: Defines the process of transitioning from OFF to SAFE.
- SAFE: The Low Voltage Power Supply but not the High Voltage Power Supply is powered. Only HK data are generated.
- CONFIGURATION: A non-observing mode for updating parameters
- MAINTENANCE: Used primarily for diagnostics
- NOMINAL: Normal data acquisition

A simplified but typical operational cycle would then consist of:

- Transition from OFF, through BOOT and into SAFE mode, loading the ASW and current parameters from Flash memory.
- Optionally go into MAINTENANCE mode as needed to address any non-routine issues.
- Go into CONFIGURATION MODE to receive TCs, update observing and calibration parameters as needed, and receive bulk science data requests (if any) for previously observed flares.
- Go into Nominal mode to acquire x-ray data, and process science data requests in background.
- Revert to SAFE mode when observing is completed
- If necessary, transition to OFF.

Notably absent are commands to adapt the data acquisition to an upcoming joint observing campaign or to solar activity. STIX basically observes in a single mode, adapting in real time to varying flux levels from current solar activity and to the current science campaign post-facto through the specification of data selection and analysis parameters. Further flexibility is provided by the ability to choose time and energy coverage and resolution, image field of view and resolution, etc. after the fact during data analysis in response to the characteristics of the flare itself and to specific science objectives. This latter capability is possible because the fundamental observables are visibilities which can be combined linearly in energy and/or time (see section 4.2). The data analysis software fully supports this flexibility.

7.2. Calibration and self-calibration

Also absent from the observing modes are any special provisions for calibration. Although aspect and routine energy and alignment calibrations are expected to be provided by the STIX team, we summarize here some elements of the energy and alignment calibration and self-calibration.

7.2.1. Energy calibration

STIX nboard data handling is based on ‘science energy channels’ (section 6.1 whose boundaries in keV must be well-matched among all detectors and pixels, Therefore it is essential that that a current energy calibration be maintained on-board to support the real-time conversions from native (ADC) channels to science energy channels (keV). This calibration is expected to drift not only over mission timescales as the detectors age and accumulate radiation damage but also on shorter timescales as the detector temperature changes. While the latter is addressed during prompt FPGA processing (section 6.1). The strategy to mitigate long term drifts employs an on-board ^{133}Ba calibration source to accumulate spectra over a multi-hour period and whose two prominent lines can be fit on the ground to yield the energy calibration gain and offset for each detector/pixel. (The response linearity is not an issue.) These parameters are then uploaded so that timely calibration information is available to the FPGA to support the conversion to keV-specified bins. While this can be a continuous process so long as STIX is observing, a significant (>1 week?) gap in observing may require operations in NOMINAL mode to acquire, process and upload calibration information prior to restarting solar observations. The operational latency between acquiring and uploading calibration data is expected to be a few days.

7.2.2. Energy self-calibration

To verify that the calibration parameters for all detectors/pixels has in fact been matched, ground analysis can exploit the fact that after calibration, the sum over any set of 4 phased pixels (A,B,C,D in figure 5) should be independent of source morphology. Thus each set, when corrected for live time and grid transmission, functions as an independent, calibrated spatially-integrated spectrometer. There are 90 such sets of independent measurements for any time interval in any flare (top, bottom and small pixels for each of the 30 Fourier subcollimators). Given the steep rise and fall in such spectra (figure xx) relative energy shifts in such spectra should provide a sensitive indication of relative errors in energy calibration gain and offset.

Some insights into inter-pixel calibration can also be obtained from the cross-check noted in Figure 5 and well as from statistical comparisons within and among flares.

Pulse pileup is a detrimental effect at high rates that is due to multiple photons interacting in a given detector pixel within the its electronic integration time. Although pulse pileup is not expected to be significant in STIX, its absence can be confirmed by comparisons of spectra formed from the large and small pixels. Since the latter are x8 smaller than the former, pileup artifacts in their spectra should be reduced by a similar factor.

7.2.3. Alignment self-calibration

Although the relative orientation and displacement of the front grid, rear grid and detectors were carefully determined during instrument assembly, one cannot rule out the possibility of changes during the mission due to thermo-elastic deformations. However, the metrology can be monitored in flight using redundancies in the flare data such as listed below:

- The relative twist orientation between the front and rear grids can affect the visibility amplitude calibration. For a known subset of subcollimators, such misalignment results in readily detectable phase shifts among the 3 redundant visibility measurements for each such subcollimator (top row, bottom row and small pixels). This provides the basis for the sensitive monitoring (and subsequent mitigtion) of the relatived orientation of the front and rear grids.
- The orientation of the individual detectors relative to the grids can be determined since each detector makes 3 independent measurements of a visibility, using the top and bottom rows of large pixels, and the set of 4 small pixels. Errors in the orientation of the detector are manifest as systematic phase shifts among the resulting 3 visibility measurements. The phase shifts should be be similar for all flares, energies and times.
- The relative displacement (parallel to the base panel) of the imager and the detector assembly has a direct effect on the measurement of visibility phase. To monitor this, the subcollimators have been divided into two uv-comparable sets: in one set a given mechanical displacement increases the measured phase; in the other, the same displacement decreases the phase. Images, independently reconstructed from each set will be best-matched when the correct relative displacement is used.

Note that corrections for moderate alignment errors can be made post facto during analysis. Unlike conventional optics, such errors do not affect image resolution or quality except for a modest impact on statistics.

7.3. Data Products

The STIX ground segment provides several levels of science data products to support a range of science analyses performed with varying degrees of calibration, continuity, and convenience. The science-related products (but not the engineering or non-routine diagnostic outputs) are now discussed.

7.3.1. Low latency pipeline

The mission's low-latency pipeline supports QL-based multi-instrument displays at the SOC to support planning activies. (see chapter xx)

The STIX input to this process is primarily spatially-integrated light curves with 4 s time resolution in 5 broad energy bands (two thermal, two non-thermal and one intermediate). In addition, for the more intense flares identified on-board, there will be rough estimates of the event location (digitized to 2 arcminutes) as well as very preliminary estimates of flare x-ray spectral parameters. This input is intended to provide indications of the timing and intensity of solar flare activity as seen from the Solar Orbiter vantage point in order to support short term mission planning and should NOT be used for science analyses.

7.3.2. Level 1 data products

Ground-generated Level 1 data products, promptly produced by the instrument team, represent the raw t/m, converted to FITS format with only basic format and units applied. This level of data serves primarily as a more convenient machine input to subsequent processing steps.

7.4. Level 2 data products

There are two classes of Level 2 data products. They differ in that the first is based exclusively on low latency t/m and so represents a complete systematic record of STIX observations. The science related subset of these products is detailed in Table xx. They will be promptly produced by the instrument team and can be considered suitable for routine scientific interpretation. The light curve and flare locations in the level 2 data have improved calibration and so effectively replace the corresponding information is the LL Pipeline. Note that there is no imaging information in this subset.

The second class of Level 2 data products are primarily derived from bulk science T/M, which is generated in response to ground-segment (or automated) data requests. As a result, they do not represent a continuous record of solar activity and may not be available until well after the event occurs. Details are shown in Table xx. The database includes the current best estimate of calibrated imaging and spectral results, made with nominal time and energy resolution. As the calibration improves, the contents of this data base may be updated from time-to-time. They will be produced by the instrument team and are fully useable for scientific interpretation. Note, howevefr, that their time and/or energy resolution may not be optimum for a given application.

7.4.1. Level 3 data products

The level 3 data products , shown in table yy, are derived from the Level 2 database and so reflect the calibration state of the Level 2 data products. These can be used for scientific analyses.

7.5. Use of STIX data products

The products outlined in the foregoing tables are intended to meet the needs of a diverse user community. The level 2 and level 3 products can be accessed either in the form of movies, images, and other displays. The corresponding digital data are also available in machine-readable form for further optimization or display by the user. Browser access to these products does

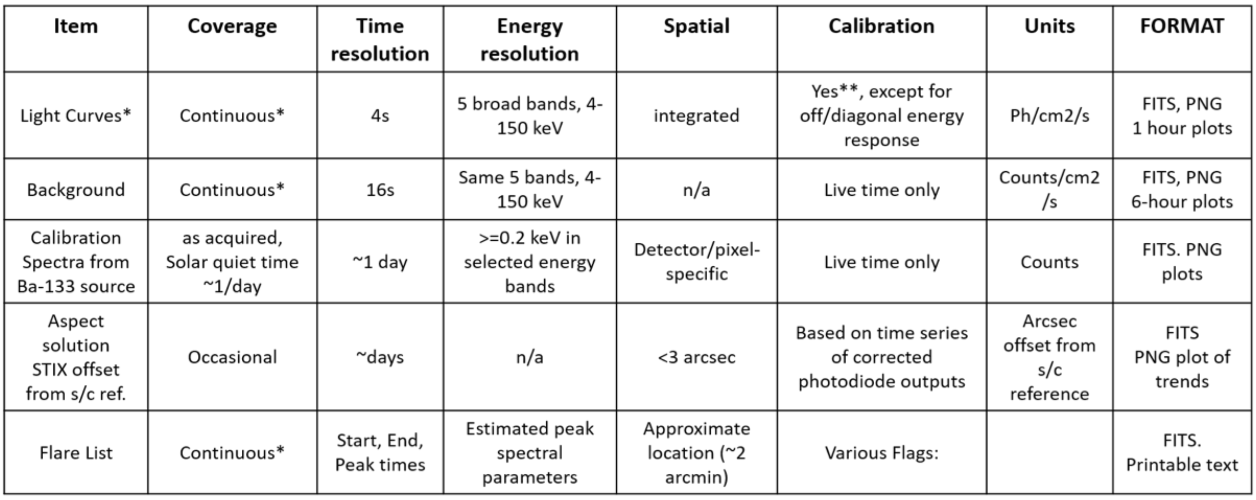

Item	Coverage	Time resolution	Energy resolution	Spatial	Calibration	Units	FORMAT
Light Curves*	Continuous*	4s	5 broad bands, 4-150 keV	integrated	Yes**, except for off/diagonal energy response	Ph/cm2/s	FITS, PNG 1 hour plots
Background	Continuous*	16s	Same 5 bands, 4-150 keV	n/a	Live time only	Counts/cm2/s	FITS, PNG 6-hour plots
Calibration Spectra from Ba-133 source	as acquired, Solar quiet time ~1/day	~1 day	>=0.2 keV in selected energy bands	Detector/pixel-specific	Live time only	Counts	FITS. PNG plots
Aspect solution STIX offset from s/c ref.	Occasional	~days	n/a	<3 arcsec	Based on time series of corrected photodiode outputs	Arcsec offset from s/c reference	FITS PNG plot of trends
Flare List	Continuous*	Start, End, Peak times	Estimated peak spectral parameters	Approximate location (~2 arcmin)	Various Flags:		FITS. Printable text

Fig. 19: Level2 QL-based Data Products

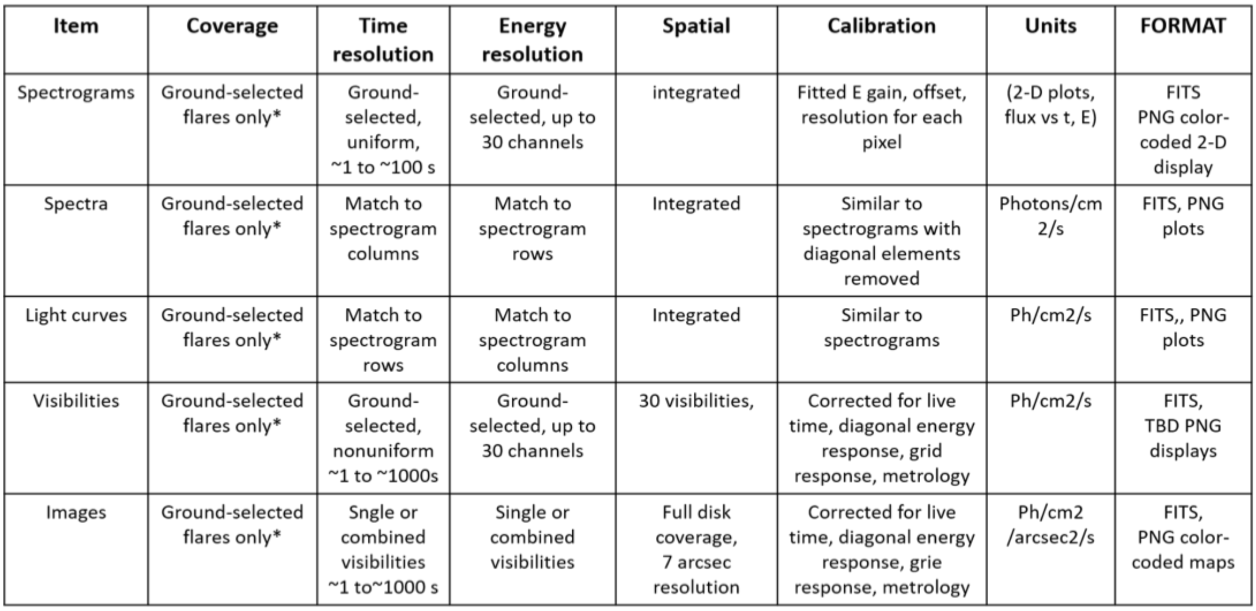

Item	Coverage	Time resolution	Energy resolution	Spatial	Calibration	Units	FORMAT
Spectrograms	Ground-selected flares only*	Ground-selected, uniform, ~1 to ~100 s	Ground-selected, up to 30 channels	integrated	Fitted E gain, offset, resolution for each pixel	(2-D plots, flux vs t, E)	FITS PNG color-coded 2-D display
Spectra	Ground-selected flares only*	Match to spectrogram columns	Match to spectrogram rows	Integrated	Similar to spectrograms with diagonal elements removed	Photons/cm2/s	FITS, PNG plots
Light curves	Ground-selected flares only*	Match to spectrogram rows	Match to spectrogram columns	Integrated	Similar to spectrograms	Ph/cm2/s	FITS,, PNG plots
Visibilities	Ground-selected flares only*	Ground-selected, nonuniform ~1 to ~1000s	Ground-selected, up to 30 channels	30 visibilities,	Corrected for live time, diagonal energy response, grid response, metrology	Ph/cm2/s	FITS, TBD PNG displays
Images	Ground-selected flares only*	Sngle or combined visibilities ~1 to~1000 s	Single or combined visibilities	Full disk coverage, 7 arcsec resolution	Corrected for live time, diagonal energy response, grie response, metrology	Ph/cm2/arcsec2/s	FITS, PNG color-coded maps

Fig. 20: Level 2 Data Products

not require specific knowledge of either the STIX hardware or software. However, their use is constrained by the fact that the parameters (e.g. time, energy resolution) has been predetermined and may therefore not fully meet the user's needs.

As a result, these databases will be supplemented by an IDL software suite, designed and documented to support users who would prefer to choose their own analysis parameters. With basic knowledge of the instrument, they can generate the customized output either by the remote use of the STIX computing facility or by installing the IDL software at their own site.

Finally, experienced users who want to extend their analysis beyond the routine level, can install the software at their own site, extend and modify it as they wish and start their analysis from the Level 1 database, using existing or redetermining calibration parameters as appropriate.

This three-fold strategy of providing the options of direct use of a calibrated data set, re-analysis with provided software tools, or direct access to the level 1 data for custom analyses is based on the approach used successfully for 17 years by the RHESSI mission.

Acknowledgements. We would like to thank the many contributors to the STIX project. Without their effort the instrument would not exist. Firstly, this includes the ESA Solar Orbiter project team, and we particularly acknowledge the support provide by Salma Fahmy, Chris Jewell, and Neil Murray. Secondly, we mention the support from your University partners, namely FHNW, . . . We also would like to thank all our industrial partners for their dedication and their effort to make STIX happen. In particular, we mention Kögl Space, Art of Technology, Almatech, ... And last but not least, we would like to thank all the funding agencies which supported STIX: Swiss Space Office, the lead funding agency for STIX, ...

References

Lin, R. P., Dennis, B. R., Hurford, G. J., et al. 2002, Sol. Phys., 210, 3
Y. Eisen et al., Nucl. Inst. and Meth. A491 (2002) 176
A. Cola, I. Farella, Appl.Phys.Lett. 94, 102113 (2009)
O. Grimm et al. 2015, JINST 10 C02011
A. Michalowska et al., Nucl. Sci. Symp. Conf. Rec. (2010) 1556-1559
A. Meuris et al. 2912, Nucl. Instr. and Meth. A695, 288-292
G. Hurford in Observing Photons in Space, ISSI(2013) Springer, New York.

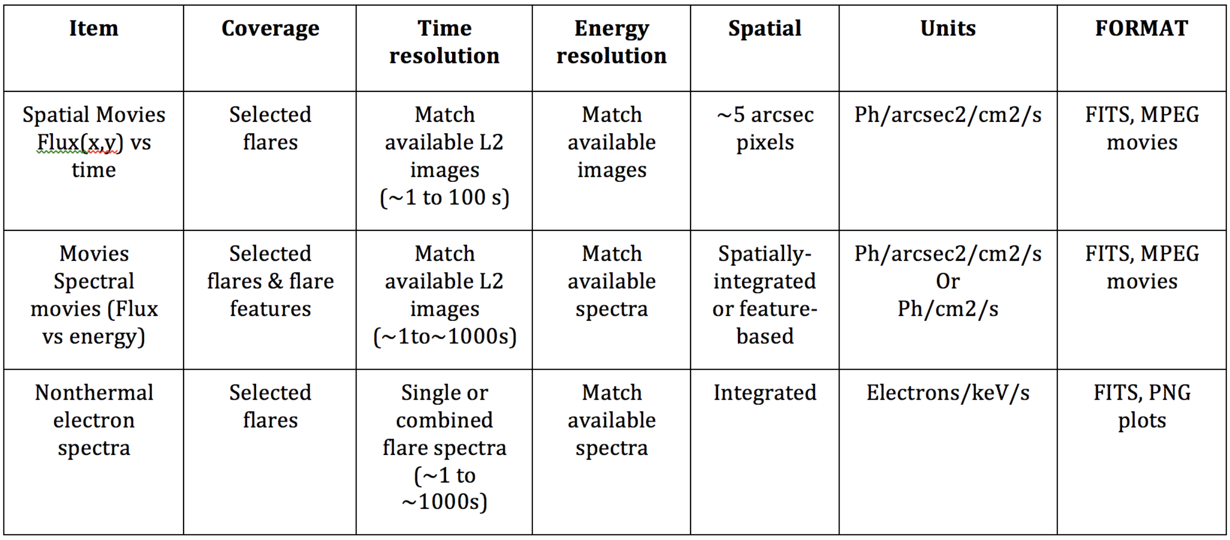

Item	Coverage	Time resolution	Energy resolution	Spatial	Units	FORMAT
Spatial Movies Flux(x,y) vs time	Selected flares	Match available L2 images (~1 to 100 s)	Match available images	~5 arcsec pixels	Ph/arcsec2/cm2/s	FITS, MPEG movies
Movies Spectral movies (Flux vs energy)	Selected flares & flare features	Match available L2 images (~1to~1000s)	Match available spectra	Spatially-integrated or feature-based	Ph/arcsec2/cm2/s Or Ph/cm2/s	FITS, MPEG movies
Nonthermal electron spectra	Selected flares	Single or combined flare spectra (~1 to ~1000s)	Match available spectra	Integrated	Electrons/keV/s	FITS, PNG plots

Fig. 21: Level 3 Data Products